J. Fluid Mech. (2009), *vol.* 624, *pp.* 69–100. © 2009 Cambridge University Press
doi:10.1017/S0022112008005326 Printed in the United Kingdom

Particle clustering in periodically forced straining flows

J. S. MARSHALL†

School of Engineering, The University of Vermont, Burlington, Vermont 05405, USA

(Received 20 April 2008 and in revised form 20 November 2008)

Numerous biomedical and industrial applications require separation or sorting of particles in systems in which it is undesirable to allow particle adhesion to a surface, such as a centrifuge wall and a filter fibre. Such systems typically involve either adhesive particles which could easily foul such surfaces or very delicate particles as is the case with suspensions of biological cells. The current study explores an approach for particle separation based on exposure to an oscillating straining flow, which would be typical for peristaltic and other types of contractive wall motions in a channel or tube. We find that particles immersed in an oscillating straining flow are attracted to the nodal points of the straining field, a phenomenon which we refer to as 'oscillatory clustering'. A simplified theory of this process is developed for cases with isolated particles immersed in an unbounded uniform straining flow, in which the particle motion is found to be governed by a damped Mathieu equation. Moreover, the drift velocity imposed on particles through oscillatory clustering is sufficient to suspend them against a downward gravitational force in a limit-cycle oscillatory path. Theoretical approximations for the average suspension height and oscillation amplitude are obtained. A discrete-element method (DEM) for colliding and adhesive particles is then employed to examine oscillatory clustering for more realistic systems in which particles collide with each other and with container walls. The DEM is used to examine oscillatory clustering of a particle suspension in an oscillating box and for standing peristaltic waves in a channel, both with and without particle adhesion forces and gravitational forces.

1. Introduction

Many applications in the chemical, food, energy and biomedical industries require a continuous process for separation of solid matter from a particulate suspension flowing through a channel or tube. Standard separation approaches include centrifugal separation, mechanical filtering and electrostatic precipitation. All of these approaches have the effect of drawing the particles towards a solid boundary, which for flows with fragile particles (e.g. biological cells) or with adhesive particles may not be desirable. Moreover, it is often easier to remove particulate matter if the particles are first encouraged to form aggregates within the flow. One common method to encourage aggregation or clustering of particles within the flow is through acoustic radiation, in which sound waves induce a radiation force on the particles of a suspension via an essentially inviscid mechanism that arises due to the fluid compressibility (King 1934). For instance, removal of particulate matter from a combustion exhaust stream can

† Email address for correspondence: jeffm@cems.uvm.edu

be enhanced by use of sound radiation to encourage aggregate formation upstream of the electrostatic precipitator (Gallego-Juárez *et al.* 1999). In this application, the sound radiation force on the particles enhances particle kinetic energy and increases the collision rate of the advected particles in the exhaust stream, thereby increasing the aggregation rate. In liquid suspensions of biological cells, ultrasonic standing waves are used to form a so-called ultrasound trap in which the acoustic radiation force induces particles to cluster at the acoustic nodal point (Spengler *et al.* 2001; Kuznetsova, Bazou & Coakley 2007). Other applications in which ultrasound waves induce separation and size sorting of rigid particles in a microchannel are described by Kapishnikov, Kantsler & Steinberg (2006).

The present paper is concerned with the effect on a particulate suspension of oscillating straining induced in an incompressible flow by wall motions in a channel. As we shall show, oscillation of the tube or channel walls provides a viable alternative to acoustic methods for manipulation of a particulate suspension, with the possibility of inducing particle separation, mixing and sorting. Unlike the acoustic radiation force, which relies on fluid compressibility effects, we consider particle drift in an incompressible fluid with viscous-dominated flow past the particles, in which particle drift arises from the slight particle inertial overshoot in the presence of the oscillating fluid velocity gradient. Surface oscillation in channel or tube flows is relatively easy to achieve in a number of transport systems. For instance, in microfluidic systems, surface oscillation can be induced by use of piezoelectric materials along the channel walls, which has led several investigators to propose peristaltic pumping as an effective means for inducing fluid transport for microfluidic circuits (Bar-Cohen & Chang 2000; Hartley 2000; Nguyen *et al.* 2002). Oscillatory wall motion is also a common driver for fluid motion in many biological flow systems, including blood transport in the vascular system, transport of bile through the bile duct into the small intestine, transport of sperm in the reproductive system, food transport in the esophagus and a wide range of processes in the digestive system.

Of these various applications, the presence of oscillating wall motions within the colon is of particular interest, since many of the various colonic contractions induce no net transport of the intestinal fluid (chyme). Nevertheless, the body continually incites contractive motions of the colon wall of several different types, in both the longitudinal and radial directions and with a range of different frequencies. Wall contractions are used in the digestive system to achieve a variety of tasks, including mixing of fluid with enzymatic secretions; mechanical, chemical and bacterial particle breakdown; particle sorting and separation; nutrient and water absorption; and material compaction of the stool (Lew, Fung & Lowenstein 1971). Within the colon, the contractions are thought to induce mixing of the suspended particles, which are generally heavier than the surrounding fluid, as well as enhancing aggregation of the particles suspended in the chyme, all while removing water from the mixture through cells embedded within the colon wall (Schulze-Delrieu *et al.* 1996). These various contractions are coordinated within the digestive system, using a local neural network, which tunes the oscillation frequency and amplitude for the given task and fluid viscosity (Gramiak, Ross & Olmstead 1971; Jouet *et al.* 1998; Putz & Pabst, 2000).

There is a large literature on fluid transport in channels and tubes driven by oscillatory wall motion, with the early work summarized in the review by Jaffrin & Shapiro (1971). The early analytical theories of peristaltic fluid transport typically utilize assumptions such as low Reynolds numbers, wall motion with wavelengths much longer than the conduit thickness and small wave amplitudes (Shapiro *et al.* 1969). Li & Brassuer (1993) extended the lubrication theory to examine effects of

unsteady flow due to arbitrary wall motion. Jaffrin (1973) developed a second-order theory for peristaltic transport with weak inertia and curvature effects and concluded that the 'inertialess' lubrication theory remains valid up to a Reynolds number of about 10. Numerical investigations of peristalsis of single-phase flows have been performed by several investigators (Takabatake & Ayukawa 1982; Pozrikidis 1987; Rathish Kumar & Naidu 1995; Natarajan & Mokhtarzadeh-Dehghan 2000), which remove some or all of the restrictions noted above. An interesting study of the effect of longitudinal motions on peristaltic pumping, with particular application to esophageal transport, is reported by Pal & Brasseur (2000, 2002), which shows that the peak pressure and shear stress in the contraction zone can be greatly reduced by local longitudinal shortening of the wall.

Many biological and industrial applications of peristaltic pumping involve transport of two different fluid phases, such as liquid and gas, liquid and solid particles, gas and solid particles and two immiscible liquids. Peristaltic pumping of annular flows with two immiscible liquids, with one liquid in a layer near the tube wall and the other in the tube centre, occurs in the gastrointestinal tract and various glandular tracts. Studies of peristalsis in two-fluid annular flows are reported by Shukla *et al.* (1980), Brasseur, Corrsin & Lu (1987), Ramachandra Rao & Usha (1995) and Usha & Ramachandra Rao (2000), and transport of two-layer power-law fluids is considered by Usha & Ramachandra Rao (1997). The motion of neutrally buoyant solid particles in a peristaltic flow during passage of a single pressure wave is examined by Hung & Brown (1976) and for a single particle in a series of peristaltic waves by Fauci (1992). An analytical model for peristaltic pumping for a suspension of particles in a fluid is considered by Srivastava & Srivastava (1989, 1997), using the assumption that the amplitude of wall motion is much smaller than the conduit width.

The current research investigates the drift, and the resulting clustering, of particles induced by an oscillating straining flow. This tendency of the particles to gather at the centre of an oscillatory straining field, referred to in this work as 'oscillatory clustering', does not appear to have been studied in any detail in previous literature. Inward lateral motion of particles is noted in passing by both Hung & Brown (1976) and Fauci (1992) in studies of particle motion during peristaltic pumping in a channel; however, the causes of this motion are not examined, and the extent and conditions for inward motion are not characterized. Neither of these papers examines the unusual oscillatory particle levitation that we observe for cases with gravitational settling in oscillating straining flows. The observation that oscillatory wall motion can be used under certain conditions to separate particles from the surrounding fluid and sort particles of different size by inducing a clustering of the particles along certain nodal points along the channel or tube centre, which is further enhanced by the presence of particle adhesion force, is of considerable relevance for explanation of a variety of biological processes in the digestive, circulatory and reproductive systems and may also have utility for potential new engineering separation processes, particularly for small-scale flow systems or systems with adhesive particles for which use of standard centrifugal separation processes might not be desirable.

In § 2 of the paper, we make use of the independence of the x and y components of the fluid velocity field for straining flows to reduce the behaviour of an isolated particle in a parametrically forced straining flow, in its simplest form, to a one-dimensional mathematical model which is governed by the damped Mathieu equation. This one-dimensional model, while neglecting important effects such as particle collision and adhesion as well as the spatial variation of straining in the tube or channel geometry, can be used to explore the response of particle dynamics as the controlling parameters

of the problem are varied. For instance, the transition from a state in which all particles cluster at the centre of the straining flow to one with different types of particle attractors, such as a central cluster surrounded by a cloud of diffuse particles, can be related using this model to the well-known instability of the damped Mathieu equation (Pritchard 1969; Taylor & Narendra 1969). We also use this model to explore the time scale associated with oscillatory clustering and the ability of the oscillatory clustering phenomenon to suspend particles in the presence of a gravitational field. In § 3, a discrete-element method (DEM) is described which is used to explore particle dynamics in parametrically forced straining flows in the remainder of the paper. Particle dynamics in an oscillating box, with a spatially uniform straining rate, is examined in § 4. In § 5, we explore particle clustering and mixing in a tube with axisymmetric contractions, resulting in a spatially varying straining rate. The effect of particle adhesive forces on particle oscillatory clustering is examined in § 6. Conclusions are given in § 7.

2. Isolated particle in an oscillating straining flow

A two-dimensional oscillatory straining flow has velocity components

$$u = s(t)x, \quad v = -s(t)y, \tag{2.1}$$

where the oscillating straining rate s can be written as the product of a constant amplitude A, with dimensions of inverse time, and a dimensionless time-varying function $f(t)$, or $s(t) = Af(t)$. The equations of motion for a small particle of mass m at a position $\boldsymbol{x}(t)$ travelling with velocity $\boldsymbol{v} = \mathrm{d}\boldsymbol{x}/\mathrm{d}t$ immersed in the flow, subject only to the Stokes drag force, is given by

$$m\frac{\mathrm{d}v}{\mathrm{d}t} = -C(\boldsymbol{v} - \boldsymbol{u}), \tag{2.2}$$

where $\boldsymbol{u}$ is the fluid velocity at position $\boldsymbol{x}$, in the absence of the particle; $C = 3\pi d\mu$ is the Stokes drag coefficient; d is the particle diameter; μ is the dynamic viscosity; and $\mathrm{d}/\mathrm{d}t$ denotes the material derivative travelling in the frame of the particle. (The added mass force can also be included simply by interpreting m as the sum of the particle mass and its added mass.) Since the x-component of velocity varies only with the x-coordinate, and similarly for the y-component, and since the momentum equation (2.2) is linear in $\boldsymbol{v}$ and $\boldsymbol{u}$, we can decompose the system (2.1) and (2.2) to write the equation of motion for each component of particle position independent of each other. For instance, the resulting governing equation for the x-component of the particle position is given by

$$\frac{\mathrm{d}^2x}{\mathrm{d}t^2} + \frac{C}{m}\frac{\mathrm{d}x}{\mathrm{d}t} - \frac{CA}{m}f(t)x = 0. \tag{2.3}$$

We consider the case of periodic straining with frequency ω, such that $f(t) = \cos(\omega t)$, and define dimensionless time and position variables by $t' = \omega t/2$ and $x' = x/L$. The characteristic fluid length scale is L, and the fluid velocity scale is $U = L\omega/2$, such that the fluid time scale is $L/U = 2/\omega$. Equation (2.3) then reduces to the dimensionless form

$$\frac{\mathrm{d}^2x'}{\mathrm{d}t'^2} + 2\zeta\frac{\mathrm{d}x'}{\mathrm{d}t'} - 2q\cos(2t')x' = 0, \tag{2.4}$$

where $\zeta \equiv C/m\omega$ and $q \equiv 2CA/m\omega^2$ are related to the particle Stokes number $St \equiv \rho_p d^2U/18\mu L$ by $\zeta = 1/(2St)$ and $q = (A/\omega)St^{-1}$. Equation (2.4) is a special form

of the damped Mathieu equation, which has the canonical form

$$\frac{\mathrm{d}^2x'}{\mathrm{d}t'^2} + 2\zeta\frac{\mathrm{d}x'}{\mathrm{d}t'} + [a - 2q\cos(2t')]x' = 0, \tag{2.5}$$

where for the present problem $a = 0$. As noted by McLachlan (1947), (2.5) can be converted into an undamped Mathieu equation for the variable $X(t')$ using the transformation $x(t') = e^{-\zeta t'}X(t')$, giving

$$\frac{\mathrm{d}^2X}{\mathrm{d}t'^2} + [\bar{a} - 2q\cos(2t')]X = 0, \tag{2.6}$$

where $\bar{a} = a - \zeta^2$. The solution of the undamped oscillator (2.6) can be either stable or unstable, depending on the value of the parameter pair $(\bar{a}, q)$. When (2.6) is stable, the solution oscillates harmonically in time, whereas when (2.6) is unstable the amplitude of oscillation increases in proportion to $\exp(\alpha t')$, where α is the instability growth rate of the undamped oscillator. Correspondingly, the solution of the damped Mathieu oscillator equation (2.5) has oscillation amplitude that decays in proportion to $\exp(-\zeta t')$ for cases in which the undamped equation (2.6) is stable and varies in proportion to $\exp[-(\zeta - \alpha)t']$ for cases in which (2.6) is unstable. The condition of marginal stability of the damped Mathieu equation occurs when the damping constant ζ is equal to the instability growth rate α of the corresponding undamped Mathieu equation (2.6).

The stability boundary of the damped Matheiu equation (2.5) can be obtained by interpolation from the stability diagram of the undamped Mathieu oscillator (McLachlan 1947, p. 98), where for the present case we have $\bar{a} = -\zeta^2$ and $\alpha_{crit} = \zeta$. A numerical method for calculation of the stability boundary of the damped Mathieu equation (2.5) is described by Robe & Jones (1975), using the Liapunov approach. A sufficient condition for asymptotic stability of the damped Mathieu equation is derived by Gunderson, Rigas & van Vleck (1974) as $q - \zeta^2 < \sqrt{a}\,\zeta$, which for the present case with $a = 0$ reduces simply to $q < \zeta^2$. We define a 'straining parameter' $S \equiv (2A/\omega)St$, where S can be interpreted as the Stokes number based on the straining amplitude A rather than the oscillation frequency ω. In terms of the straining parameter, this sufficient condition for stability reduces to $S < 1/2$.

We solve (2.4) for the time variation of the particle position for different values of the straining parameter S and the dimensionless frequency $b \equiv 1/\zeta$. Equation (2.4) is solved using a fourth-order Runge–Kutta method with initial conditions $x' = 1$ and $\mathrm{d}x'/\mathrm{d}t' = q/\zeta = 2S/b$, which are equivalent to choosing the fluid length scale L as the initial particle displacement and setting the initial particle velocity equal to the fluid velocity at the particle centroid. All computations are performed with time step size $\Delta t' = 0.01$, which provides over 300 time steps per oscillation.

The inward drifting of particles in an oscillating straining flow occurs due to the effect of particle inertia under the influence of the oscillating fluid velocity field. As shown in figure 1(*a*), the particle velocity lags the fluid velocity at the particle position by a small amount due to the particle inertia. The consequence of this velocity lag is demonstrated in figure 1(*b*), where we compare the position of a particle with that of a passive marker (which is inertialess) released at the same initial position, given by $x'(T) = \exp[(S/b)\sin(bT)]$, where $T \equiv 2t'/b = Ct/m$ is a scaled time variable. The fluid velocity is initially upward, causing the position of both the particle and the passive marker to increase above the initial particle position. However, the particle inertia causes the particle to rise slightly higher than the passive marker at the top of the arc, as the direction of straining changes sign. Since the particle position is slightly

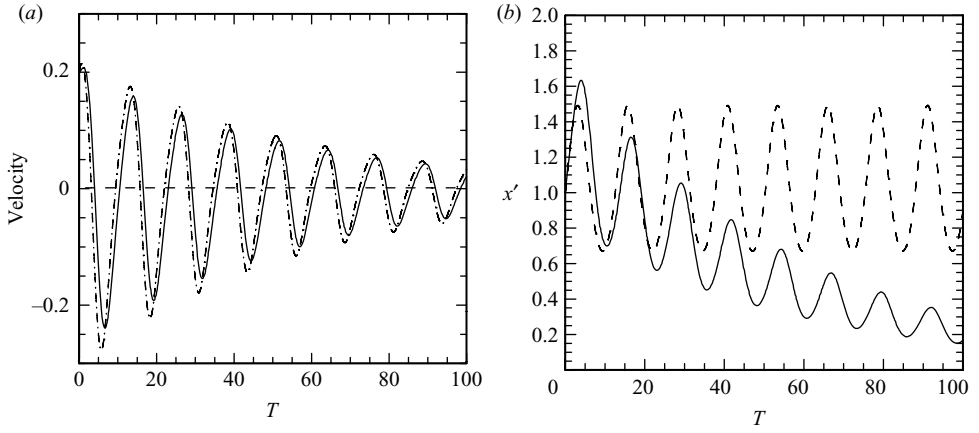

FIGURE 1. Plots showing (a) particle velocity (solid line) and the fluid velocity at the particle position (dashed–dotted line) and (b) position of a passive particle (dashed line) and a real particle (solid line) for a case with $S = 0.2$ and $b = 0.5$.

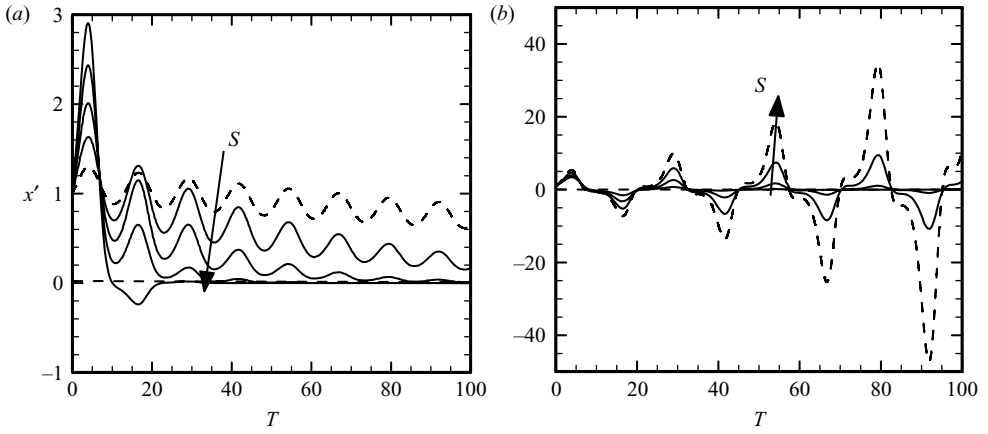

FIGURE 2. Plots showing particle displacement $x(t)$ for cases with $b = 0.5$ and different values of S: (a) medium straining parameter values $S = 0.1$, 0.2, 0.3, 0.4, 0.5 and (b) high straining parameter values $S = 0.6$, 0.7, 0.8, 0.9. A dashed line is used to denote cases with $S = 0.1$ and $S = 0.9$.

higher than the passive marker in figure 1(b) at the point at which the downward fluid velocity is the maximum, the negative peak in velocity in figure 1(a) at $T \sim 6$ has a larger magnitude than the initial upward velocity. After the direction of straining changes again and the particle moves back upward, the opposite occurs – the particle lags behind the passive marker such that the maximum upward velocity at $T \sim 12$ is less than the initial velocity value. This cycle continues to repeat itself, with the negative velocity peaks being less than the corresponding positive velocity peaks due to the lag induced by the particle inertia, leading to a velocity bias that generates a downward average particle velocity.

The governing equation for the particle position becomes unstable as S is increased. In figure 2 we plot particle position at dimensionless frequency $b = 0.5$ for different values of S, with cases for $0.1 \leqslant S \leqslant 0.5$ in figure 2(a) and cases with $0.6 \leqslant S \leqslant 0.9$ in figure 2(b). From the sufficient condition of Gunderson *et al.* (1974), the solution of

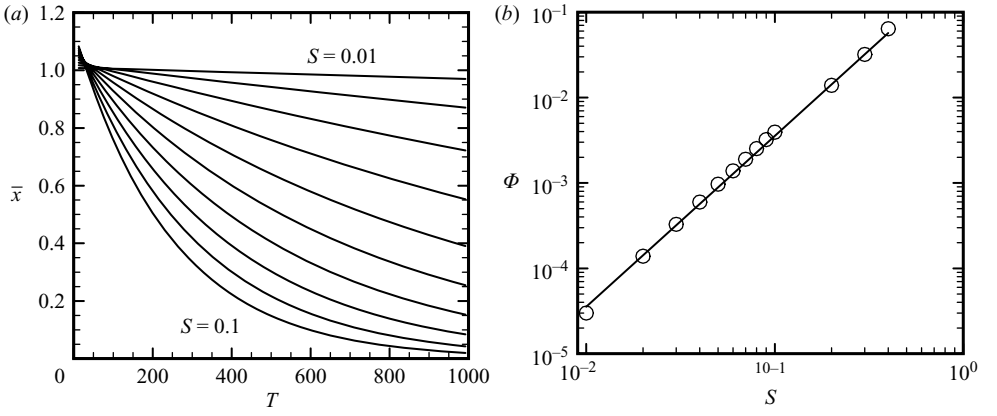

FIGURE 3. Plots showing (*a*) exponential form of decay of the phase-averaged particle position for cases with $b = 0.5$ and $S = 0.01$–0.1, with increments of 0.01 and (*b*) clustering rate Φ as a function of straining parameter, showing computational data (symbols) and curve fit $\Phi = 0.356\,S^2$ (line).

the damped Mathieu equation for the particle position will be asymptotically stable for all values of b whenever $S < 0.5$. The results in figure 2(*a*), as well as our results for a wide variety of other frequency values, are consistent with this prediction. As S increases in the interval $0.1 \leqslant S \leqslant 0.5$, the height of the particle position peak near time $T \sim 4$ increases, and then the rate at which the particle approaches the centre of straining ($x = 0$) also increases. For the case with $S = 0.5$, the particle overshoots $x = 0$ to attain a negative value of position before returning to nearly zero. For cases with $S > 0.5$, the stability of the particle motion depends on the frequency value. In the cases shown in figure 2(*b*), the particle overshoots the centre of straining at regular intervals. The overshoot amplitude diminishes slowly with time for $S = 0.6$ and 0.7, but for the $S = 0.8$ and 0.9 cases it increases with time, indicative of system instability.

An approximate solution for the rate at which particles approach the nodal point of the straining flow can be obtained for small Stokes numbers, using the locally implicit equilibrium Euler approximation introduced by Ferry *et al.* (2003). In this approximation, the particle momentum equation (2.2) is given by

$$\boldsymbol{v} = \boldsymbol{u} - \frac{m}{C}\frac{\mathrm{d}\boldsymbol{v}}{\mathrm{d}t} \cong \boldsymbol{u} - \frac{m}{C}\frac{\mathrm{D}\boldsymbol{u}}{\mathrm{D}t} + O(St)^2, \tag{2.7}$$

where the $\mathrm{D}/\mathrm{D}t$ notation in the last term denotes the material derivative following the fluid. Applying this approximation to our one-dimensional model and averaging the resulting expression for particle velocity over the oscillation period of the straining flow yields an expression for the dimensionless particle drift velocity $\bar{v}$ as

$$\bar{v} = \mathrm{d}\bar{x}/\mathrm{d}t' = -(S^2/b)\bar{x}, \tag{2.8}$$

where $\bar{x}$ is the phase-averaged dimensionless particle position (i.e. the particle position averaged over the oscillation period). Integration of (2.8) yields

$$\bar{x}(t') = \exp[-(S^2/b)t']. \tag{2.9}$$

The decay rate of the particle position is examined by numerical solution of (2.4) for cases with $0.01 \leqslant S \leqslant 0.5$ over a long time period $0 < T < 1000$ with $b = 0.5$ (figure 3*a*). For each case, the phase-averaged particle position $\bar{x}$ can be fit using an exponential

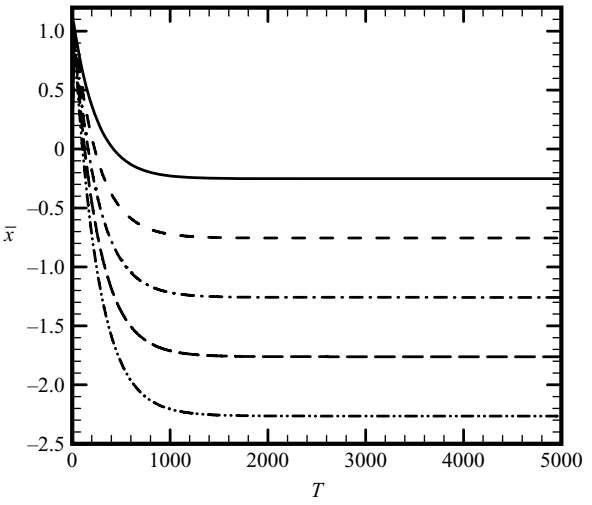

FIGURE 4. Plots showing the effect of downward gravitational force on the phase-averaged particle position for cases with $S = 0.1$, $b = 0.5$ and $Fr = 7.91$ (solid line), 4.56 (short dashed line), 3.53 (dashed–dotted line), 2.99 (long dashed line) and 2.63 (dashed–dotted–dotted line).

function of the form

$$\bar{x}(t') = \exp(-\varphi\, t') = \exp(-\Phi T), \tag{2.10}$$

where $\Phi = b\varphi/2$. The constant φ is called the 'clustering rate' and when measured from the computational data with $b = 0.5$ is found to be closely approximated by a power-law fit of the form

$$\varphi \cong 0.71 S^2/b. \tag{2.11}$$

For instance, in figure 3(b) we show the observed values of clustering rate versus the fit $\Phi \cong 0.356\, S^2$, which is equivalent to (2.11), on a log–log plot with data for nearly two decades in S values, yielding a linear fit with slope equal to 2. The data fit (2.11) has the same dependence on S and b as the vanishing Stokes number approximation (2.9) but with about a 30% difference in the coefficient.

In the presence of downward gravitational settling, the model equation (2.4) becomes

$$\frac{\mathrm{d}^2 x'}{\mathrm{d}t'^2} + 2\zeta \frac{\mathrm{d}x'}{\mathrm{d}t'} - 2q\cos(2t')x' = -1/Fr^2, \tag{2.12}$$

where $Fr \equiv U/\sqrt{g_R L} = (\omega/2)\sqrt{L/g_R}$ is the Froude number; $g_R \equiv g(1-\chi)$ is the reduced gravitational acceleration; and $\chi \equiv \rho_f/\rho_p$ is the fluid-to-particle density ratio. We perform a series of computations of (2.12) with different values of Fr to examine the ability of the oscillatory clustering phenomena to suspend particles against a mean downward gravitational force, where the phase-averaged particle position $\bar{x}(t')$ is plotted in figure 4 for $Fr = 2.63$, 2.99, 3.53, 4.56 and 7.91. All values of Fr examined exhibit suspension of the downward gravitational settling by the upward motion of the particle induced by the oscillatory clustering mechanism. Over a long time, the particle exhibits a limit-cycle behaviour with amplitude ψ and centred at some (negative) mean value of x, denoted by $\bar{x}_\infty$. The smaller the value of Fr, the further the centre of the limit cycle from the centre of straining and the larger the amplitude of particle oscillations in the limit cycle.

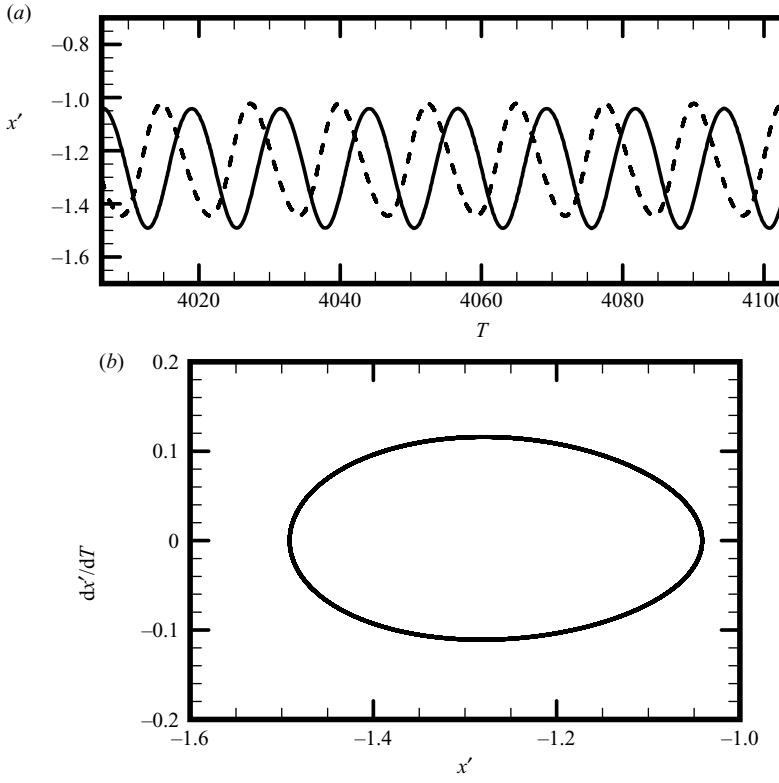

FIGURE 5. Motion of a particle in time over several oscillation periods (a) in physical space and (b) in phase space over the time interval $4000 \leqslant T \leqslant 4100$, for a case with $S = 0.1$, $b = 0.5$ and $Fr = 3.53$. In (a), the dashed curve denotes the function $0.2\cos(bT) - 1.25$, which oscillates in phase with the forcing function.

A plot showing the motion of a particle over several oscillation periods and the corresponding limit-cycle behaviour in phase space are given in figures 5(a) and 5(b), respectively. In figure 5(a), the solid line denotes the particle path in the limit-cycle mode, and the dashed line is a function that oscillates in phase with the forcing function $\cos(bT)$. We observe that the particle oscillates with the same frequency as the forcing function but with a different phase. The orbit of the particle in phase space is plotted in figure 5(b) over the time increment $4000 \leqslant T \leqslant 4100$ and is found to form a closed curve indicative of limit-cycle behaviour.

In order to derive expressions for the mean height $\bar{x}_\infty$, oscillation amplitude ψ and phase C of the particle limit cycle, we assume that the particle position oscillates periodically with frequency b and apply the Fourier series decomposition as

$$x'(t') = \bar{x}_\infty + A_1 \sin(2t') + B_1 \cos(2t') + \sum_{n=2}^{\infty} B_n \cos(2nt' + C_n). \tag{2.13}$$

Equating the dominant $n = 1$ terms of the Fourier series with a function of the form $\psi\cos(2t' + C) = \psi\cos(C)\cos(2t') - \psi\sin(C)\sin(2t')$, we associate the A_1 and B_1 coefficients of the Fourier series with the limit cycle amplitude ψ as $B_1 = \psi\cos(C)$ and $A_1 = -\psi\sin(C)$. Substituting (2.13) into (2.12) and integrating over the interval

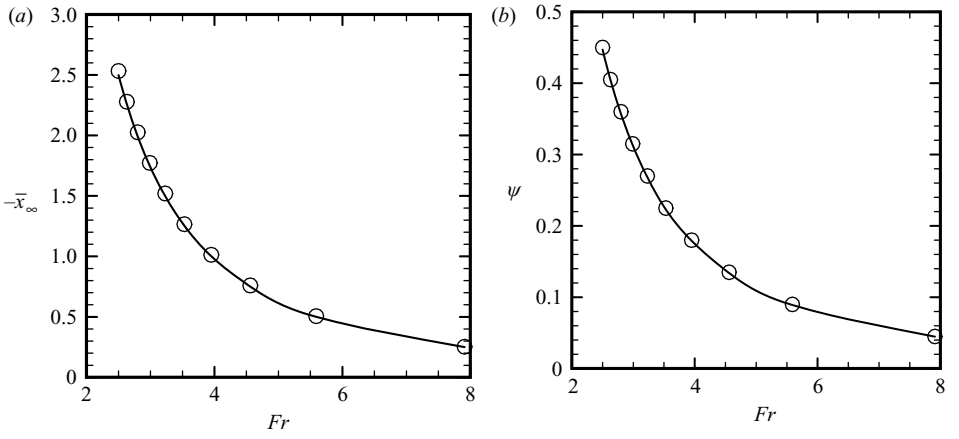

FIGURE 6. Characteristics of the limit-cycle oscillations for a particle suspended under gravity by oscillatory clustering for a case with $S = 0.1$ and $b = 0.5$, showing (a) mean suspension height $\bar{x}_\infty$ and (b) oscillation amplitude ψ as functions of the Froude number. Symbols denote computational data, and lines are the theoretical predictions from (2.16) and (2.17).

$(t', t' + \pi)$ yields the result $B_1 = 1/(q\,Fr^2)$; so the limit cycle amplitude becomes

$$\psi = 1/[qFr^2\cos(C)]. \tag{2.14}$$

Substituting (2.13) into (2.12), multiplying the result by $\sin(2t')$ and then integrating over $(t', t' + \pi)$ yields a solution for the phase C as

$$\tan C = \zeta. \tag{2.15}$$

From (2.15) we can write $\cos C = (1 + \zeta^2)^{-1/2}$, so that the solution (2.14) for limit cycle amplitude becomes

$$\psi = \frac{(1+\zeta^2)^{1/2}}{q\,Fr^2} = \frac{b(1+b^2)^{1/2}}{2\,S\,Fr^2}. \tag{2.16}$$

Substituting (2.13) into (2.12), multiplying by $\cos(2t')$ and integrating over $(t', t' + \pi)$ yields a solution for the asymptotic phase-averaged particle position, $\bar{x}_\infty$, as

$$\bar{x}_\infty = -\frac{2(1+\zeta^2)}{q^2Fr^2} = -\frac{b^2(1+b^2)}{2S^2Fr^2}. \tag{2.17}$$

The predictions (2.16) and (2.17) are compared to the computational data in figure 6 for the different values of Fr plotted in figure 5, with $S = 0.1$ and $b = 0.5$, and are found to be an almost exact match to the data.

3. Discrete-element method (DEM)

The simplified model discussed in § 2 neglects a number of important effects, such as particle collisions and adhesive force, which lead to a coupling of the particle dynamics in different dimensions. Further, the simplified model is not appropriate for problems such as periodic contractions of a tube, since the flow field is more complicated than the simply straining flow given in (2.1). In order to test applicability of the results of the simplified model to these more realistic problems, we perform a series of computations using a soft-sphere DEM for adhesive particles, the details of

which are described in this section. A similar computational method has been used by the author in previous papers (Marshall 2007; Li & Marshall 2007; Zhao & Marshall 2008), and so only a summary is given here.

These DEM computations are implemented in a multiple-time-step algorithm, which employs three time steps to resolve processes of the order of the fluid time scale $T_F = L/U$, the particle time scale $T_P = d/U$ and the collision time scale $T_C = d(\rho_P^2/E_P^2 U)^{1/5}$, where E_P is the particle elastic modulus. Further increase in computational efficiency is obtained for the problem of particles in an oscillating tube by advecting the particles on a Cartesian grid and using a level-set function to represent the tube boundaries within the Cartesian grid (Mousel 2006). In the problems examined in this paper, the fluid flow is prescribed, and the particles are assumed not to affect the fluid flow.

The DEM solves the linear and angular momentum equations

$$m\frac{\mathrm{d}\boldsymbol{v}}{\mathrm{d}t} = \boldsymbol{F}_F + \boldsymbol{F}_A, \quad I\frac{\mathrm{d}\boldsymbol{\Omega}}{\mathrm{d}t} = \boldsymbol{M}_F + \boldsymbol{M}_A \tag{3.1}$$

for each particle in the system, where $\boldsymbol{v}$ and $\boldsymbol{\Omega}$ are the particle velocity and rotation rate; $\boldsymbol{F}_F$ and $\boldsymbol{F}_A$ are the fluid forces and the lumped collision and adhesion forces; and $\boldsymbol{M}_F$ and $\boldsymbol{M}_A$ are the fluid and lumped collision and adhesion torques. Particles moving in a viscous fluid are subject to a variety of forces, including lift, drag, added mass, buoyancy and Magnus and gravity forces (Maxey & Riley 1983). The relative contribution of these forces to the total fluid force exerted on a particle is dependent on dimensionless parameters such as the dimensionless particle diameter $\varepsilon \equiv \mathrm{d}/L$, the fluid-to-particle density ratio $\chi = \rho_F/\rho_P$, the dimensionless shear parameter $B \equiv \omega L^2/\nu$ and the particle Reynolds number $Re_p \equiv |v-u|d/\nu$, where ω is the fluid vorticity magnitude and ν is the kinematic fluid viscosity. In what follows, it is assumed that ε and Re_p are much less than unity. The dominant force in most flows with small particle Reynolds number is the fluid drag. For instance, the ratio of the lift and Magnus forces to the drag force scale as $O(\varepsilon B^{1/2})$ and $O(\varepsilon B)$, respectively, and the ratio of the buoyancy and added mass forces to the particle inertia scales as $O(\chi)$. Assuming that the particles are small compared with the flow dimensions ($\varepsilon \ll 1$) and that the vorticity is limited by the viscous boundary layer scaling ($B \leqslant O(1)$), the lift and Magnus forces can be neglected.

For particles with small ε and Re_p, the drag force is given by

$$\boldsymbol{F}_d = -3\pi d\mu(\boldsymbol{v}-\boldsymbol{u})f. \tag{3.2}$$

The Stokes drag solution for an isolated sphere is recovered for $f = 1$. A correction proposed by Di Felice (1994) to account for particle crowding in non-dilute flows is used with $f = (1-c)^{-3.7}$, where $c(\boldsymbol{x}, t)$ is the local equivalent three-dimensional particle concentration. The area-based particle concentration $\bar{c}$ is determined by spreading the cross-sectional area of each particle in a 'cloud' with radius R_n, selected to be the average separation distance between the particle and the nearest four particles, and with Gaussian distribution function $D(x-x_n) = (1/\pi R_n^2)\exp[-|x-x_n|^2/R_n^2]$. The cloud amplitude $A_n = \pi d^2/4$ for two-dimensional flows is set equal to the area of the particle projection on the plane of motion. Summing over the contributions of the nearby particle clouds yields the area-based concentration $\bar{c}(\boldsymbol{x}, t)$:

$$\bar{c}(x, t) = \sum_{n=1}^{N} A_n D(x - x_n, R_n). \tag{3.3}$$

The equivalent three-dimensional concentration field $c(\boldsymbol{x}, t)$ is obtained by requiring that the two- and three-dimensional cases have the same ratio of the characteristic particle separation distance ℓ to the particle diameter, which yields $c = (4/3\pi^{1/2})\bar{c}^{3/2}$.

The fluid-induced viscous torque $\boldsymbol{M}_F$ arises from a disparity between the particle and fluid rotation rates, and is given by

$$\boldsymbol{M}_F = \pi\mu d^3\left(\frac{1}{2}\boldsymbol{\omega} - \boldsymbol{\Omega}\right). \tag{3.4}$$

The reduced gravity force $\boldsymbol{F}_g$, pressure gradient force $\boldsymbol{F}_p$ and added mass force $\boldsymbol{F}_a$ are given by

$$\boldsymbol{F}_g = m(1-\chi)\boldsymbol{g}, \quad \boldsymbol{F}_p = \chi\, m\frac{\mathrm{D}\boldsymbol{u}}{\mathrm{D}t}, \quad \boldsymbol{F}_a = -c_M\chi\, m\left(\frac{\mathrm{d}\boldsymbol{v}}{\mathrm{d}t} - \frac{\mathrm{d}\boldsymbol{u}}{\mathrm{d}t}\right), \tag{3.5}$$

where $\boldsymbol{g}$ is the gravitational acceleration vector; $\mathrm{D}/\mathrm{D}t$ denotes the rate of change with time following a fluid particle; and the added mass coefficient for a sphere is $c_M = 1/2$.

Colliding particles experience a normal force from elastic particle deformation, as well as resistance responses related to sliding and rolling. Some of the computations presented in this paper also involve adhesive force between the particles, whereas other computations do not. In the present section we provide the full DEM theory including adhesive forces. The theory without adhesive forces can be obtained as a limiting case of the theory presented here, and the 'adhesionless' theory has also been described in another recent publication (Marshall 2006). The total collision and adhesion force and torque fields on particle i with radius r_i are given by

$$\boldsymbol{F}_A = F_n\boldsymbol{n} + F_s\boldsymbol{t}_S, \quad \boldsymbol{M}_A = r_i F_s(\boldsymbol{n}\times\boldsymbol{t}_S) + M_r(\boldsymbol{t}_R\times\boldsymbol{n}), \tag{3.6}$$

where $\boldsymbol{n} = (\boldsymbol{x}_j - \boldsymbol{x}_i)/|\boldsymbol{x}_j - \boldsymbol{x}_i|$ is the unit normal vector oriented along the line connecting the centres of the two colliding particles, i and j. The sliding resistance acts in a direction $\boldsymbol{t}_S$, corresponding to the direction of relative motion of the particle surfaces at the contact point projected onto the contact plane (the plane orthogonal to $\boldsymbol{n}$). The sliding resistance also imposes a torque on the particle in the $\boldsymbol{n}\times\boldsymbol{t}_S$ direction. The rolling resistance exerts a torque on the particle in the $\boldsymbol{t}_R\times\boldsymbol{n}$ direction, where $\boldsymbol{t}_R$ is the direction of the 'rolling' velocity.

The normal elastic force of two colliding particles can be expressed in terms of the effective radius R and the effective elastic and shear moduli, E and G, defined by

$$\frac{1}{R} \equiv \frac{1}{r_i} + \frac{1}{r_j}, \quad \frac{1}{E} \equiv \frac{1-\sigma_i^2}{E_i} + \frac{1-\sigma_j^2}{E_j}, \quad \frac{1}{G} \equiv \frac{2-\sigma_i}{G_i} + \frac{2-\sigma_j}{G_j}, \tag{3.7}$$

where E_i, σ_i and r_i are the elastic modulus, Poisson ratio and radius of particle i, respectively. The adhesive force between the two particles depends on the surface potential γ, where the work required to separate two spheres colliding over a contact region of radius $a(t)$ is given by $2\pi\gamma\, a^2$ in the absence of further elastic deformation. The normal particle force is further decomposed into an elastic part F_{ne} and a dissipative part F_{nd}. The elastic part of the normal force can be expressed in terms of the contact region radius $a(t)$ and the particle overlap δ_N by (Chokshi, Tielens & Hollenbach 1993)

$$\frac{\delta_N}{\delta_C} = 6^{1/3}\left[2\left(\frac{a}{a_o}\right)^2 - \frac{4}{3}\left(\frac{a}{a_o}\right)^{1/2}\right], \quad \frac{F_{ne}}{F_C} = 4\left(\frac{a}{a_o}\right)^3 - 4\left(\frac{a}{a_o}\right)^{3/2}, \tag{3.8}$$

where the particle overlap δ_N is defined by

$$\delta_N = r_i + r_j - |\boldsymbol{x}_i - \boldsymbol{x}_j| \,. \tag{3.9}$$

The critical overlap δ_C, the critical normal force F_C and the equilibrium contact radius a_o are given by (Johnson, Kendall & Roberts 1971)

$$F_C = 3\pi\gamma R, \quad \delta_C = \frac{a_o^2}{2(6)^{1/3}R}, \quad a_o = \left(\frac{9\pi\gamma R^2}{E}\right)^{1/3}. \tag{3.10}$$

As two particles move away from each other, they remain in contact until $F_{ne} = -F_C$ and $\delta_N = -\delta_C$ due to the necking within the contact region caused by particle adhesive forces. Beyond this state any further separation leads the two particles to break apart. In the limit of no adhesive force, (3.8) reduces to the classic particle repulsion force formula of Hertz (1882).

In addition to the normal adhesive force, we employ a normal dissipative force to account for the fact that colliding particles at sufficiently low Stokes number, below about $St = 10$, exhibit no rebound due to the viscous fluid forces between the particles (Joseph *et al.* 2001). The dissipative part of the normal force (F_{nd}) is given by

$$F_{nd} = -\eta_N \boldsymbol{v}_R \cdot \boldsymbol{n}, \tag{3.11}$$

where $\boldsymbol{v}_R = \boldsymbol{v}_{Ci} - \boldsymbol{v}_{Cj}$ is the relative particle surface velocity at the contact point; $\boldsymbol{v}_{C,i} = \boldsymbol{v}_i + \boldsymbol{\Omega}_i \times \boldsymbol{r}_i$ is the surface velocity of particle i at the contact point; $\boldsymbol{r}_i = r_i \boldsymbol{n}$ and $\boldsymbol{r}_j = -r_j \boldsymbol{n}$ are the vectors from the particle centroids to the contact point; and η_N is the normal damping coefficient. Tsuji, Tanaka & Ishida (1992) propose a form for the damping coefficient as

$$\eta_N = \bar{\alpha}(m k_N)^{1/2}, \tag{3.12}$$

where $k_N = (4/3)E\,a(t)$ is the normal stiffness coefficient. For cases with zero restitution coefficient, the coefficient $\bar{\alpha} \cong 1.27$.

The presence of particle adhesion leads to a torque that resists particle rolling. For uniform-size spherical particles, the 'rolling velocity' $\boldsymbol{v}_L$ of particle i is given by (Bagi & Kuhn 2004)

$$\boldsymbol{v}_L = -R(\boldsymbol{\Omega}_i - \boldsymbol{\Omega}_j) \times \boldsymbol{n}. \tag{3.13}$$

We express the rolling resistance torque M_r as a linear function of the particle rolling displacement $\xi = (\int_{t_0}^{t} \boldsymbol{v}_L(\tau)d\tau) \cdot \boldsymbol{t}_R$ in the 'rolling direction' $\boldsymbol{t}_R = \boldsymbol{v}_L/|\boldsymbol{v}_L|$, such that

$$M_r = -k_R\,\xi. \tag{3.14}$$

Rolling involves an upward motion of the particle surfaces within one part of the contact region and a downward motion in the other part of the contact region. The presence of an adhesion force between the two contacting surfaces introduces a torque resisting rolling of the particles. An expression for the rolling resistance due to van der Waals adhesion was derived by Dominik & Tielens (1995), which yields the coefficient k_R as

$$k_R = 4F_C(a/a_0)^{3/2}. \tag{3.15}$$

Dominik & Tielens (1995) further argue that the critical resistance occurs when the rolling displacement ξ achieves a critical value, corresponding to a critical rolling angle $\theta_{crit} = \xi_{crit}/R$. For $\xi > \xi_{crit}$, the rolling displacement ξ in (3.14) is replaced by ξ_{crit}.

Small particles at low particle Reynolds number do not slide significantly, so we select a fairly simple form for the sliding resistance, which primarily serves to suppress

sliding motion. The effect of van der Waals adhesion on tangential sliding force was examined by Savkoor & Briggs (1977), and a simplified model was proposed by Thornton (1991). In the sliding resistance model employed in this paper, a springlike expression for the sliding resistance of the form (Cleary, Metcalfe & Liffman 1998)

$$F_s = -k_T \left(\int_{t_0}^{t} \boldsymbol{v}_S(\xi) d\xi \right) \cdot \boldsymbol{t}_S \tag{3.16}$$

is used when the resistance force is less than a critical value F_{crit}. Here the slip velocity $\boldsymbol{v}_S(t)$ is the tangent projection of $\boldsymbol{v}_R$ to the particle surface at the contact point, or $\boldsymbol{v}_S = \boldsymbol{v}_R - (\boldsymbol{v}_R \cdot \boldsymbol{n})\boldsymbol{n}$, and the slip direction is $\boldsymbol{t}_S = \boldsymbol{v}_S / |\boldsymbol{v}_S|$. An expression for the tangential stiffness coefficient k_T is derived by Mindlin (1949), which can be written in terms of the contact region radius $a(t)$ as $k_T = 8Ga(t)$. The critical sliding force is approximated using the expression

$$F_{crit} = \mu_f \, |F_{ne} + 2F_C| \,, \tag{3.17}$$

where F_C is given in (3.10) and μ_f is the friction coefficient. The expression (3.17) was shown by Thornton (1991) to provide results in reasonable agreement with experiments. For $|F_s| \geqslant F_{crit}$, the sliding resistance is given by the Amonton expression $F_s = -F_{crit}$.

4. Oscillating uniform straining flow

In order to evaluate the influence of collisions on the oscillatory clustering phenomenon, we perform two-dimensional computations in a box with oscillatory compression in the x- and y-directions. For the flow field given by the periodic straining flow (2.1) with dimensionless straining rate $s(t) = (2S/b)\cos(2t')$, the box boundaries are specified by

$$x_B = \pm \exp[(S/b)\sin(2t')], \quad y_B = \pm \exp[-(S/b)\sin(2t')]. \tag{4.1}$$

The particles were initially placed on an array covering the inside of the box, and then the particle position was randomly perturbed by a small amount, with maximum perturbation equal to about 20% of the initial particle separation distance. The particle initial velocity was set equal to the local fluid velocity.

The transport of particles is controlled by a number of dimensionless parameters. For adhesionless flow, these parameters include the dimensionless particle diameter $\varepsilon \equiv d/L$, an elasticity parameter $\lambda \equiv E/\rho_p U^2$, the average effective volume-based particle concentration c_0 and the density ratio χ, Stokes number St, Froude number Fr and dimensionless straining amplitude S and frequency b defined in § 2. The characteristic fluid velocity is chosen as $U = L\omega/2$, and the fluid length scale L is set equal to half the initial width of the box. The values of these parameters are selected in the present section to be typical of an aqueous solution with particles that are close to neutrally buoyant. For all cases considered, we set $\varepsilon = 0.01$, $\chi = 0.99$, $\bar{c}_0 = 0.05$ (corresponding to an effective three-dimensional concentration $c_0 = 0.008$) and $\lambda = 10^4$ and vary the values of S, b and Fr as indicated in table 1.

A multiple-time-step scheme is used to solve for the particle motion and collisions, with a fluid time step Δt, a particle time step Δt_P and a collision time step Δt_C. Using the time scales given in § 3, these time steps can be related to governing the dimensionless parameters by $\Delta t/\Delta t_P = O(1/\varepsilon)$ and $\Delta t_P/\Delta t_C = O(\lambda^{2/5})$. Based on the typical values listed in table 1, we choose $\Delta t/\Delta t_P = 10$ and $\Delta t_P/\Delta t_C = 40$.

Case	S	b	Fr	Case	S	b	Fr
A1	0.1	0.5	∞	B1	0.2	0.5	8
A2	0.2	0.5	∞	B2	0.2	0.5	5
A3	0.3	0.5	∞	B3	0.2	0.5	3
A4	1.0	0.5	∞	B4	0.2	0.5	2
				B5	0.2	0.5	1

TABLE 1. Parameters used for computation of particles in an oscillating box. For all cases, $\varepsilon = 0.01$, $\chi = 0.99$, $\overline{c}_0 = 0.05$ and $\lambda = 10^4$.

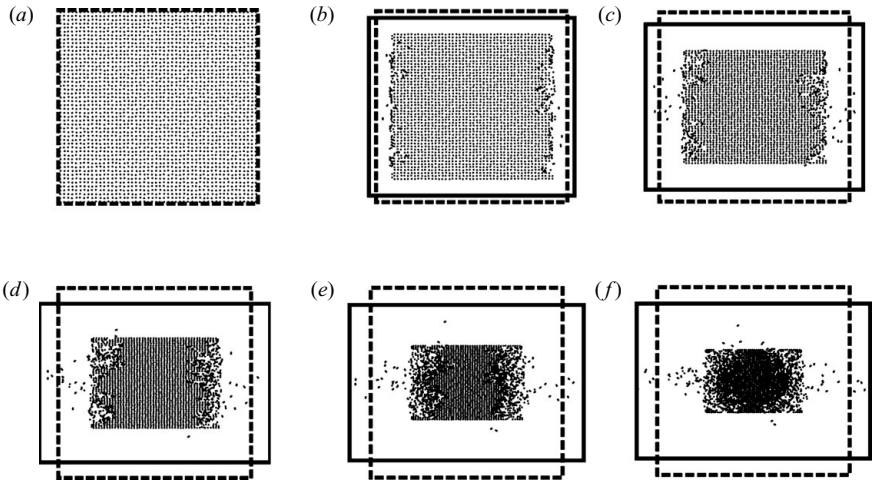

FIGURE 7. Time series showing oscillatory clustering of particles for case A1 after every 10 oscillations, at times (*a*) $t = 0$, (*b*) 31.6, (*c*) 63.2, (*d*) 94.8, (*e*) 126.4 and (*f*) 158. The box positions are drawn at the current time (solid line) and at $t = 0$ (dashed line).

The dimensionless fluid time step is set as $\Delta t = 0.01$. In the following, time is non-dimensionalized by $L/U = 2/\omega$, such that the dimensionless oscillation period is equal to π for all cases, and all velocities and length variables are non-dimensionalized by U and L, respectively.

A time series showing the effects of oscillatory clustering on the particle positions for a case with $S = 0.1$ and $b = 0.5$ (case A1) is given in figure 7. The figure plots the particle positions in intervals of approximately 10 oscillation cycles, where the particle box at the time corresponding to the particle positions is indicated by a solid line, and the initial particle box is indicated by a dashed line. The particle array compresses in a nearly homogeneous reduction in spacing between particles, although the ordered array of particles is broken up on the left and right sides, where the particles have collided with the box sides due to inertial overshoot during the first oscillation. As time passes, the particles continue to cluster in a progressively more concentrated region near the centre of oscillation, until they finally reach the point of maximum concentration, beyond which further constriction is limited by particle collision.

Contraction of the particles is measured by the root mean square (r.m.s.) particle position in the x- and y-directions. In figure 8 we plot time variation of y_{rms} for cases A1–A4, with straining parameter values of $S = 0.1$, 0.2, 0.3 and 1, respectively. The particle positions at time $t = 200$, after over 60 oscillation cycles, for cases A1–A3 are plotted in figure 9. For these cases, the particles contract into a diamond pattern

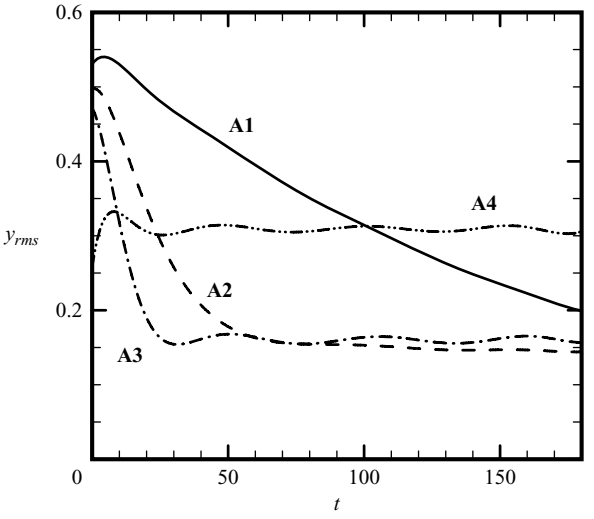

FIGURE 8. Plots of r.m.s. value of the particle y-positions for cases A1 (solid line), A2 (short dashed line), A3 (dashed-dotted line) and A4 (long dashed line), fit by a 10th-order polynomial.

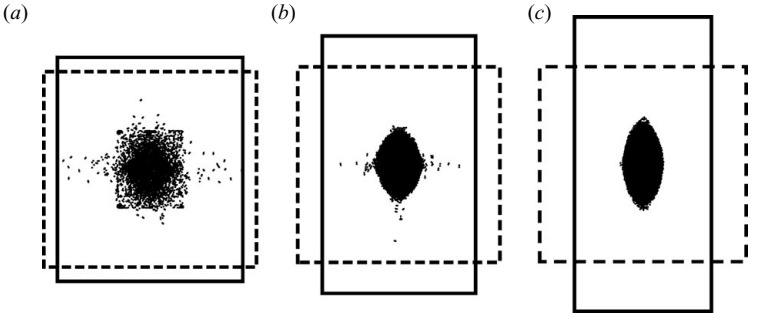

FIGURE 9. Plots of particle positions at $t = 200$ for cases (a) A1, (b) A2 and (c) A3. The dashed rectangle is the original box position, and the solid rectangle is the box position at time $t = 200$.

centred at the origin, in which the particles are packed to the maximum concentration. The diamond shape periodically stretches in the x- and y-directions in phase with the compression and elongation of the box. Once this limiting state is attained, the values of x_{rms} and y_{rms} oscillate about a constant mean value, and no further net contraction of the particles is possible. As predicted by the simple one-dimensional theory in § 2, the clustering rate increases with increase in the straining parameter S, up to the limiting value of S for stability of the system.

The diamond shape observed for the particle clusters forms due to the combination of the inward particle drift, particle collision forces and imposed oscillating flow field. The collision forces for cases with no adhesion include the elastic and dissipative normal forces and the sliding resistance. The normal forces serve primarily to restrict inward motion of the particles so as to limit particle overlap. Sliding resistance exerts a torque on the particles that leads to rotation of particles relative to each other and subsequent deformation of the cluster by particle rolling. However, computations performed for case A3 both with and without sliding resistance exhibit nearly identical results, indicating that the form of the cluster is not sensitive to the form of the expressions used for collision forces.

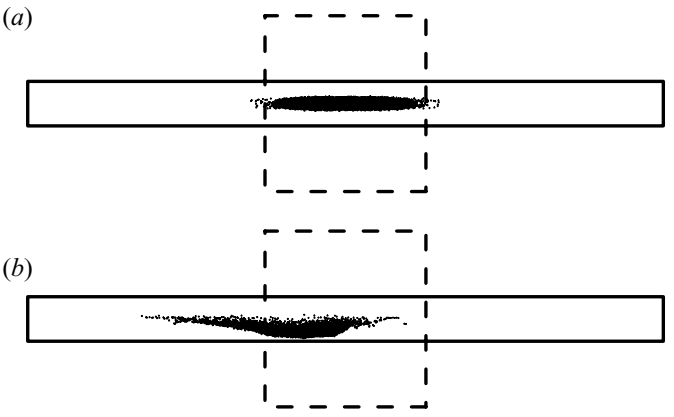

FIGURE 10. Particle positions at $t = 200$ for case A4 (a) with modification of particle drag to account for crowding and (b) with isolated particle drag expression ($f = 1$). The dashed rectangle is the original box position, and the solid rectangle is the box position at time $t = 200$.

Case A4, with $S = 1$, exhibits rather different behaviour from the other three cases, which is perhaps associated with the observation that the corresponding damped Mathieu equation (2.4) is unstable for this case (see figure 3b). For this case the values of x_{rms} and y_{rms} exhibit nearly constant oscillation amplitude and mean value with time. The particle positions form a very elongated cluster within the box, as seen in figure 10(a). We find that the form of the particle cluster for cases in which the corresponding Mathieu equation is unstable can be significantly influenced by the particle crowding modification to the drag force. To illustrate this point, we repeated the computation in case A4, using the particle drag expression for isolated particles (i.e. setting $f = 1$ in 3.2). The corresponding form of the particle cluster using the isolated particle drag expression is shown in figure 10(b). For the latter case, the particles do not cluster in the centre of the straining flow, and they also do not mix throughout the box. They instead stretch outward in a highly concentrated, wavy sheet which oscillates back and forth in the x- and y-directions with the oscillations of the box. The particles are nearly touching each other within this sheet, but they exhibit no tendency to gather near the box centre. These computations, as well as other cases examined with unstable Mathieu equation, suggest that modifications to the drag due to particle crowding may in some cases be able to stabilize the particle dynamics to the effects of instability in the corresponding Mathieu equation in the isolated particle model.

Based on the theory in § 2, the oscillatory clustering phenomenon is expected to suspend particles against the gravitational force for cases in which the limit-cycle centroid position $\bar{x}_\infty > -1$, which from (2.17) yields a criterion for particle suspension at some distance above the bottom of the box as

$$Fr > Fr_{crit} = \frac{\sqrt{2}}{q}(\zeta^2 + 1)^{1/2} = \frac{b(1 + b^2)^{1/2}}{\sqrt{2}\,S}. \tag{4.2}$$

We examine a series of computations (cases B1–B5) for $S = 0.2$ and $b = 0.5$, with different values of Fr. The box motion is identical for all five of these cases. For these values of S and b, the critical Froude number from (4.2) is $Fr_{crit} = 1.98$. For all cases examined, it is found that after a short transient the particles enter into a limit-cycle behaviour which is repeated for the remainder of the computation. Plots

		Theory		Computation: average particle y-position			
Case	Fr	Suspension height ($-\bar{x}_\infty$)	Oscillation amplitude (ψ)	Minimum	Maximum	Average	Amplitude
B1	8	0.06	0.022	0.018	0.043	0.029	0.013
B2	5	0.16	0.056	0.046	0.12	0.077	0.037
B3	3	0.43	0.16	0.15	0.38	0.25	0.12
B4	2	0.98	0.35	0.28	0.69	0.46	0.21
B5	1	3.9	1.4	0.58	1.31	0.91	0.37

TABLE 2. Comparison of theoretical predictions for particle suspension height ($-\bar{x}_\infty$) and oscillation amplitude (ψ) from (2.16) to (2.17) with computational values for an oscillating box at different Froude numbers. Cases B4 and B5 have Froude number at or below the critical value.

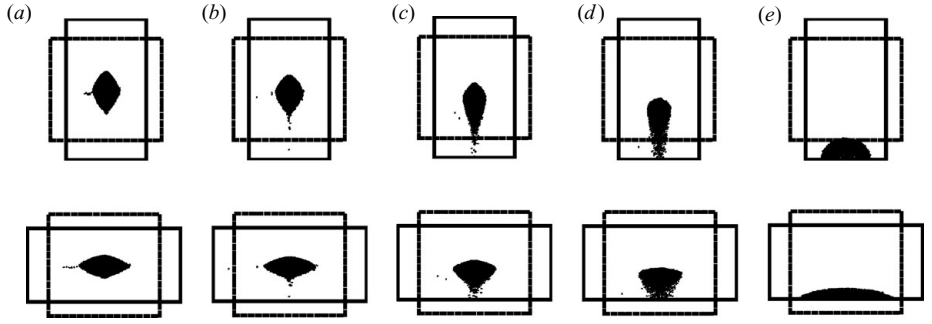

FIGURE 11. Plots of particle positions at two times separated by a half-period – $t = 498.42$ (top row) and $t = 499.98$ (bottom row) – for cases with different Froude numbers (*a*) B1, (*b*) B2, (*c*) B3, (*d*) B4 and (*e*) B5. Rectangles denote box position at the current time, and square boxes denote the initial box position.

of the particle positions at two times during this limit cycle, separated by half of an oscillation period, are shown in figure 11. The average suspension height and the range of particle positions for these five cases are listed in table 2.

For cases B1–B3, the Froude number is above the critical value, and the particles are suspended at a position above the bottom surface of the box. For large Froude numbers the effect of gravity is small, and so the particles form a diamond shape that oscillates with the box, similar to that observed for case A2 with no gravity. As the Froude number is decreased in case B3, the diamond begins to deform, and the top part of the diamond drops downward with the bottom part elongating downward and reaching almost the bottom of the box at each oscillation cycle. For case B4, the Froude number is exactly at the critical value, and we see that the upward transport of the particles via oscillatory clustering is no longer sufficient to suspend them off the bottom surface of the box. The particles are compressed in the y-direction due to oscillatory clustering, so that they fall within a semi-clustered region that extends downward to the bottom box surface, stretching up and down with each box oscillation. For case B5, the Froude number is half of the critical value, and the particles are seen to form a heap that sits at the bottom of the box. This heap grows wider as the box moves upward and thinner as the box moves downward in response to the straining flow in the x-direction.

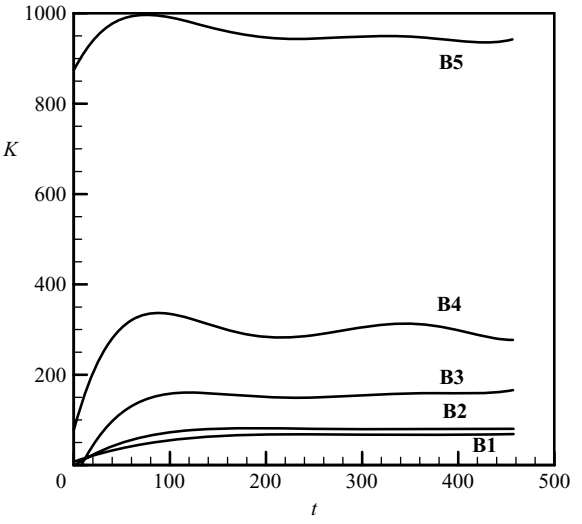

FIGURE 12. Time variation of maximum granular kinetic energy K for cases B1–B5, fit using a fifth-order polynomial.

The theoretical values for suspension height and oscillation amplitude from (2.16)–(2.17) are listed in table 2 for cases B1–B5. These values are compared to the maximum, minimum and mean value over time and the amplitude of variation of the spacially averaged y-position of the particles, where the time averaging is performed over the interval $t > 300$ for which the particles have achieved a limit-cycle configuration. For the three cases B1–B3 with Froude number above the critical value, the oscillation amplitude compares reasonably well with the theoretical values from (2.16). The predicted particle suspension height from (2.17) is somewhat above the interval of oscillation of average particle position in the DEM computations for these cases. We note that the inclusion of the particle crowding correction in the particle drag equation has a substantial effect on lowering the amplitude of oscillation and in particular in decreasing the maximum value of $-y_{ave}$. Runs with the same parameter values but without this crowding correction term yield values fairly close to the theoretical predictions. For cases B4 and B5, the Froude number is at or below the critical value, and the oscillation amplitude and mean particle height are both less than the predicted theoretical values for an unbounded domain. This result is expected for this case due to particle collision with the bottom surface of the box.

The granular kinetic energy of the particles, $K \equiv 0.5|\boldsymbol{v} - \bar{\boldsymbol{v}}|^2$, is determined for all cases by computing the spatially averaged particle velocity field $\bar{\boldsymbol{v}}$ on a 100×100 grid at each time step and then evaluating K in each grid cell. Within the region occupied by the particle clusters, the granular kinetic energy is the strongest in the region farthest from the centre of straining in the y-direction. This observation is consistent with the prediction from § 2 that the particle oscillation amplitude ψ increases with distance away from the centre of straining. The magnitude of the granular kinetic energy also increases with decrease in the Froude number, as demonstrated in the plot of maximum value of granular kinetic energy (fit using a fifth-order polynomial to smooth out fluctuations) versus time in figure 12 for cases B1–B5. The farther the average particle position away from the centre of the box the higher the granular kinetic energy.

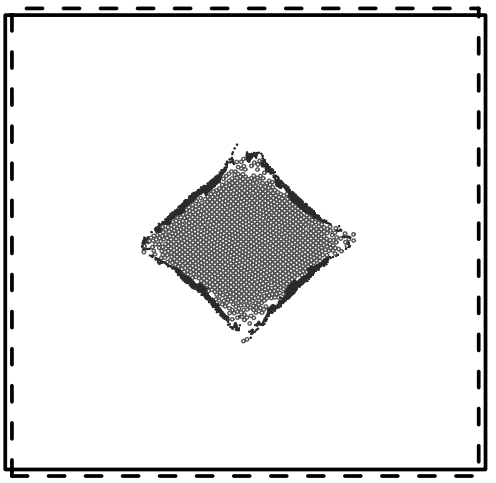

FIGURE 13. Plot showing positions of particles with diameter $d/L = 0.015$ (grey) and diameter $d/L = 0.005$ (black) for a case with $S = 0.2$, $b = 0.5$ and no gravity, at time $t = 800$.

The effect of oscillatory clustering for a case with two different particle sizes is examined for $S = 0.2$ and $b = 0.5$, where we use equal number of particles of diameters $d_1 = 0.005$ and $d_2 = 0.015$ initially arranged in a staggered pattern on a grid. In agreement with the theory in § 2, the larger particles respond more quickly to the oscillation of the straining field, since they have nearly nine times the Stokes number of the smaller particles. The larger particles quickly move through the field of smaller particles and cluster into a diamond shape at the centre of the box, similar to that shown in figure 9(*b*), leaving the smaller particles behind in a disorganized cloud. The smaller particles also eventually move towards the box centre due to oscillatory clustering, at a much slower rate than the larger particles, and deposit on the sides of the diamond-shaped cluster formed of large particles, as shown in figure 13. This computation demonstrates that oscillatory clustering can not only be used to separate particles from a fluid in which they are suspended but that it also serves as a potential approach for fabrication of structured particle aggregates with layers differentiated by particle Stokes number.

5. Particle dynamics subject to periodic contractions in a channel

The current section investigates particle clustering in a peristaltic contractile flow with no net transport, which exemplifies a flow with an oscillatory but non-uniform straining rate. This flow is also of practical interest as an idealization of phasic contractions observed in the colon. The flow field is solved using the lubrication theory, which requires that the flow Reynolds number $Re_F = UL/\nu = \omega L^2/2\nu$ and the wavenumber $k \equiv 2\pi L/\lambda$ are small compared to unity. In practice, however, it is noted by Jaffrin (1973) that the lubrication assumption remains reasonably valid for peristaltic flows even for non-small values of the flow Reynolds number up to about 10. The current analysis for peristaltic motion follows a similar approach to that used by Li & Brasseur (1993).

We consider a two-dimensional channel which is periodic with length λ and half-width L and no net flow within the channel. The channel side walls are symmetrically perturbed, such that at time t the side walls are at $y = \pm h(x, t)$. The governing

equations for the lubrication approximation are

$$\frac{\partial u}{\partial x}+\frac{\partial v}{\partial y}=0, \quad \frac{\partial p}{\partial x}=\mu\frac{\partial^2 u}{\partial y^2}, \tag{5.1}$$

subject to the condition of periodic over length λ in the x-direction and the boundary conditions

$$u(x,h,t)=0, \quad v(x,h,t)=\frac{\partial h}{\partial t},$$

$$\frac{\partial u}{\partial y}(x,0,t)=0, \quad v(x,y,t)=0. \tag{5.2}$$

Integrating the momentum equation in (5.1) twice over y and using (5.2) yields the parabolic profile

$$u(x,y,t)=-\frac{h^2-y^2}{2\mu}\frac{\partial p}{\partial x}. \tag{5.3}$$

Substituting this result into the continuity equation and integrating over y, making the usual assumption that pressure is a function of x and t, yields an expression for the vertical velocity component as

$$v(x,y,t)=\frac{h}{\mu}\left(\frac{h}{2}\frac{\partial^2 p}{\partial x^2}+\frac{\partial h}{\partial x}\frac{\partial p}{\partial x}\right)y-\frac{y^3}{6\mu}\frac{\partial^2 p}{\partial x^2}. \tag{5.4}$$

Imposing the kinematic boundary condition (5.2) yields an equation for pressure gradient as

$$\frac{h^3}{3}\frac{\partial^2 p}{\partial x^2}+h^2\frac{\partial h}{\partial x}\frac{\partial p}{\partial x}=\mu\frac{\partial h}{\partial t}. \tag{5.5}$$

Integrating this equation once over x yields

$$\frac{\partial p}{\partial x}=\frac{1}{h^3}\left[G_0(t)+3\mu\int_0^x\frac{\partial h}{\partial t}(s,t)\,\mathrm{d}s\right], \tag{5.6}$$

where the function $G_0(t)$ depends on the phase of the channel wall motion. The condition of periodicity over the wavelength λ leads to the compatibility condition

$$\int_0^\lambda\frac{\partial h}{\partial t}(s,t)\,\mathrm{d}s=0, \tag{5.7}$$

which must be satisfied by the channel wall motion in order for mass to be conserved.

We now consider standing waves on the channel of the form

$$h(x,t)=L+H\cos(\omega t)\cos(kx). \tag{5.8}$$

For waves of this form, the pressure gradient vanishes at $x=0$, so $G_0(t)=0$. Substituting (5.8) into (5.6) and (5.5) gives

$$\frac{\partial p}{\partial x}=-\frac{3\mu\omega H}{kh^3}\sin(\omega t)\sin(kx), \tag{5.9a}$$

$$\frac{\partial^2 p}{\partial x^2}=-\frac{3\mu\omega H}{h^3}\left[\sin(\omega t)\cos(kx)+\frac{3H}{2h}\sin(2\omega t)\sin^2(kx)\right]. \tag{5.9b}$$

Substitution of (5.9*a*,*b*) into (5.3) and (5.4) yields the fluid velocity field associated with the wall motion (5.8).

The length and velocity variables are non-dimensionalized using the channel width as the fluid length scale L and $U = \omega L/2$ as the fluid velocity scale. Time is non-dimensionalized by the convective time scale $L/U = 2/\omega$. We define a dimensionless wavenumber $\alpha \equiv kL = 2\pi L/\lambda$ and an amplitude ratio $\eta \equiv H/L$. In terms of these variables, the dimensionless velocity components become

$$u' = \frac{3\eta}{\alpha h'}\left(1 - \frac{y'^2}{h'^2}\right)\sin(2t')\sin(\alpha x'), \tag{5.10a}$$

$$v' = -3\eta\frac{y'}{h'}\left(1 - \frac{y'^2}{h'^2}\right)\sin(2t')\cos(\alpha x') - \frac{3}{2}\frac{\eta^2}{h'}\frac{y'}{h'}\left(1 - \frac{3y'^2}{h'^2}\right)\sin(4t')\sin^2(\alpha x'), \tag{5.10b}$$

where dimensionless variables are denoted with primes. We perform computations over one period of a standing wave field, with dimensionless wavelength $\lambda = 10$ (corresponding to $\alpha = 0.63$) and amplitude ratio $\eta = 0.4$. The flow Reynolds number $Re_F = 20$, which is similar to that observed for contractions of the colon (Jaffrin 1973). No gravitational force was used in the computation. The straining flow field has nodal points at the start and end of the period and at the mid-period location, corresponding to $x = 0$, 5 and 10. The Stokes number is related to the particle size and flow Reynolds number by $St = \varepsilon^2 Re_F/18\chi$.

Two sets of computations were performed: one for 'fine' particles with $\varepsilon \equiv d/L = 0.02$ and one for 'coarse' particles with $\varepsilon = 0.1$. The straining parameter S and frequency parameter b at the nodal points of the peristaltic channel flow are related to the Stokes number by $S = 3\eta St$ and $b = 2St$. In the computation with fine particles, the Stokes number is so small (0.0004) that very little clustering of the particles is observed. The computation with the coarse particles had a larger Stokes number (0.01), and the oscillatory clustering was clearly visible. For instance, in figure 14 we plot the particle positions at four different times, over which the channel walls oscillate nearly one hundred times. The particles are initially uniformly distributed on an array throughout the channel, with average area-based concentration $\bar{c}_0 = 0.19$ (and an effective volume-based concentration $c_0 = 0.06$). Oscillatory clustering causes the particles both to move in the horizontal (x-) direction towards the nodal points and to contract in the vertical (y-) direction at the nodal point locations. The vertical contraction is limited by particle contact, such that at the final time a bridge forms connecting the particles both above and below the nodal points. The r.m.s. value of the vertical (y) position of the particles is plotted versus time in figure 15, which exhibits a slow decrease in time as the particles contract towards the nodal points of the straining field.

6. Effect of particle adhesion force

We have observed in the previous sections that oscillating straining flows cause particles to cluster at the nodal points of a straining flow and that the rate of clustering is greater for larger particle sizes (with higher Stokes numbers). We now examine the effect of particle adhesion on this phenomenon. In particular, we are interested in whether particle adhesion increases the clustering rate and in the structure of the particle aggregates that form in an oscillating straining flow. A van der Waals adhesion force is imposed between the particles in this study, using the theory developed in § 3. We denote by A the effective Hamaker constant for the interaction of two similar particles through a fluid medium. If δ denotes the characteristic

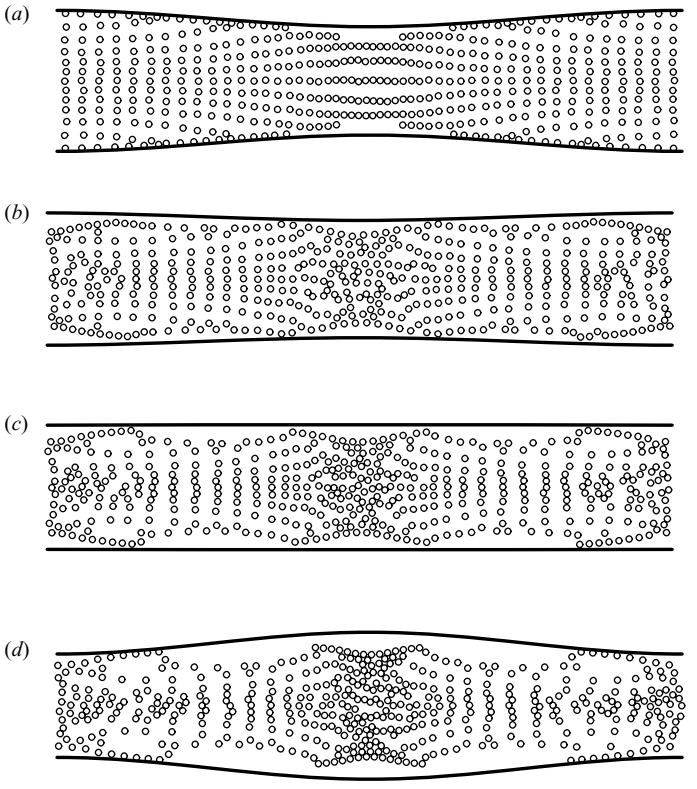

FIGURE 14. Particle positions and channel wall locations for periodic peristaltic contractions of a channel with amplitude ratio 0.4 and wavelength 10, with plots given at (*a*) $t = 0.6$, (*b*) $t = 99.8$, (*c*) $t = 198.7$ and (*d*) $t = 299.5$.

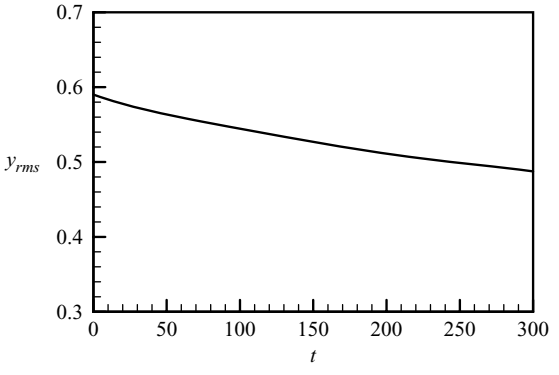

FIGURE 15. Decay of r.m.s. *y*-coordinate of particles with time for the same case as described for figure 14, fit using a fifth-order polynomial.

minimum separation distance of two particle surfaces within the contact region, the effective surface potential γ can be related to A by

$$\gamma = \frac{1}{2}\int_{\delta}^{\infty} \frac{A}{6\pi h^3}\,\mathrm{d}h = \frac{A}{24\pi\,\delta^2}, \tag{6.1}$$

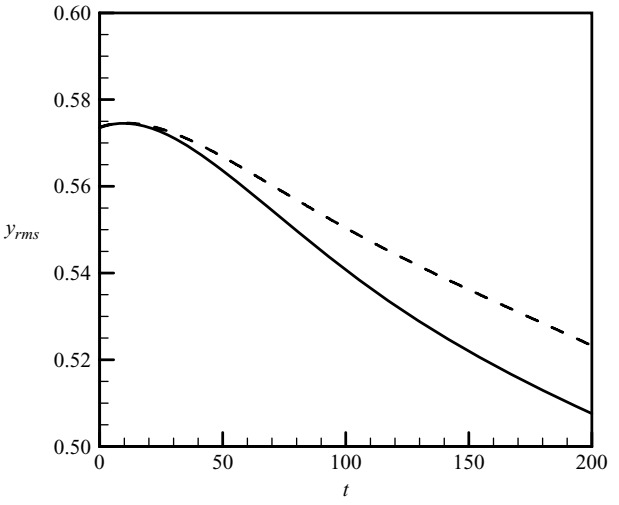

FIGURE 16. Comparison of r.m.s. y-position of particles for an oscillating box with no adhesion (dashed line) and with adhesion (solid line). Curves are fit using a 10th-order polynomial.

where $A/6\pi h^3$ is the van der Waals force per unit area between two infinite plates separated by a distance h. From a computational study of the elastohydrodynamic response of two colliding particles, Serayssol & Davis (1986) show that the minimum separation distance between two colliding particles scales as $\delta \approx (\mu U d^{3/2}/2\pi E)^{2/5}$. This estimate is found by Serayssol & Davis (1986) not to change significantly with addition of adhesive forces between the surfaces. We employ a dimensionless 'adhesion parameter' to characterize the magnitude of particle adhesive force relative to the particle inertia, which is defined by

$$\phi \equiv \frac{\gamma}{\rho_p U^2 R}. \tag{6.2}$$

We first examine the effect of adhesion on particle motion in an oscillating box, with $S = 0.01$, $b = 0.05$, $\varepsilon = 0.01$ and an average area-based particle concentration $\bar{c}_0 = 0.2$ (corresponding to an effective volume-based concentration $c_0 = 0.065$). For these low values of S and b, the particles exhibit relatively slow clustering. Two computations were conducted, one with no adhesion and one with adhesion parameter $\phi = 10$, where for the adhesive case particles were not allowed to adhere to the box walls. A comparison of the r.m.s. value of the y-position of the particles for both of these cases is given in figure 16. The value of y_{rms} oscillates in phase with the box oscillation, so we have fit a tenth-order polynomial to each curve to eliminate the high-frequency oscillations. The value of y_{rms} decreases more rapidly for the case with adhesion during most of the computation.

A time series showing the formation of aggregates is given in figure 17. The aggregates first form on the sides of the box, where the amplitude of particle oscillation is the largest. They have a dendritic structure, stretching inward towards the centre of straining. With each oscillation of the box, additional particles collide with and are captured by these dendritic structures, leaving a small particle-free region surrounding each particle aggregate. As this process continues over time, an increasing percentage of the particles are captured, and the aggregates grow to such an extent that they connect with one another. Over a long time a quasi-stationary state is reached in

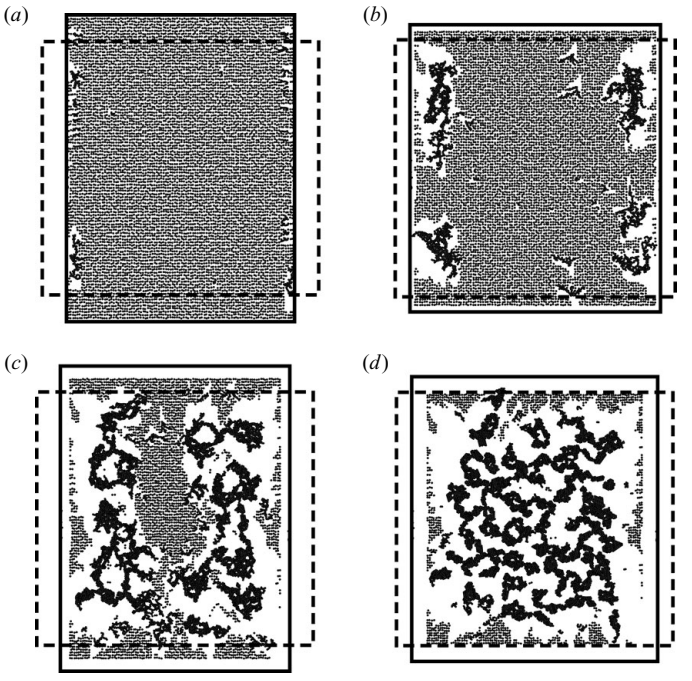

FIGURE 17. Time series showing particle positions and box locations at the current time (solid) and the initial time (dashed) for a case with particle adhesion at times (*a*) $t = 21.1$, (*b*) 71.0, (*c*) 200.5 and (*d*) 379.1.

which the particles are contained in a loose mesh of connecting aggregates, thus inhibiting further contraction of the structure towards the centre of straining due to aggregate contact. This aggregate mesh breaks into smaller pieces periodically at certain contact points as the particles are advected by the oscillating straining flow, only to reconnect at these points after the straining flow has reversed.

The effect of particle adhesion for peristaltic oscillations in a channel are examined for a case with amplitude ratio $\eta = 0.4$, dimensionless wavelength $\lambda = 10$ (corresponding to $\alpha = 0.63$), particle radius $\varepsilon = 0.02$, flow Reynolds number $Re_F = 10$ and average area-based particle concentration $\bar{c}_0 = 0.13$ (corresponding to an effective volume-based concentration of $c_0 = 0.035$). For this case the particle Stokes number is $St = 3 \times 10^{-4}$, so the rate of clustering is expected to be small. Computations are performed with no adhesion and with adhesion parameter values of $\phi = 10$, 40 and 100. A comparison of the r.m.s. values of the particle y-position for the case with no adhesion and that with $\phi = 10$ is given in figure 18, where a 10th-order polynomial is fit to the curves to smooth out the oscillations arising from the peristaltic contractions. The values of y_{rms} for the cases with $\phi = 40$ and 100 are almost identical to that with $\phi = 10$. The case with no adhesion exhibits an initial reduction in y_{rms}, after which it appears to be nearly flat, indicating negligible particle clustering towards the nodal points of the straining field. The cases with adhesion, on the other hand, exhibit a steady reduction in y_{rms} with time, although the rate of clustering is still small.

A plot showing particle positions at time $t = 498.8$, after about 159 oscillation periods, is given in figure 19 for cases with $\phi = 0$ (no adhesion), 10 and 100. The lines in the plots indicate the wall positions at the given time. All cases exhibit a reduction

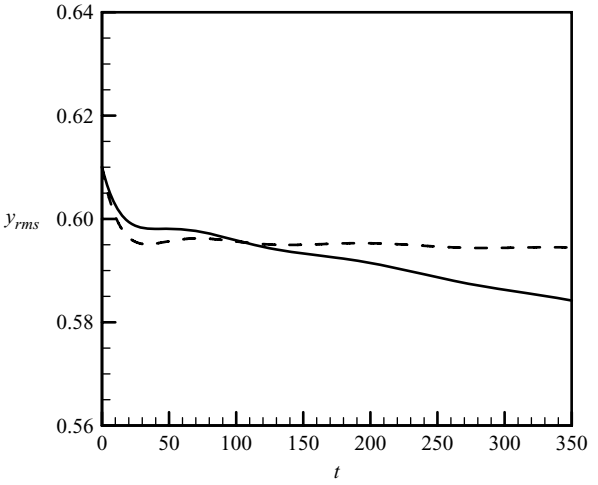

FIGURE 18. Comparison of r.m.s. y-position of particles for peristaltic oscillations with no adhesion (dashed line) and with adhesion parameter $\phi = 10$ (solid line) for a case with $\eta = 0.4$, fit using 10th-order polynomials.

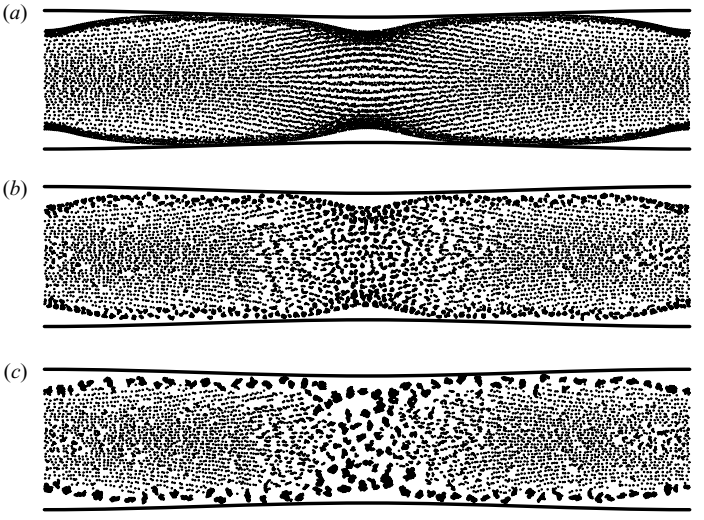

FIGURE 19. Comparison of particle positions for peristaltic oscillations (a) with no adhesion, (b) with adhesion parameter $\phi = 10$ and (c) with adhesion parameter $\phi = 100$ at time $t = 498.8$. Solid lines indicate the current position of the channel walls.

in particle y-positions near the nodal positions at $x = 0$, 5 and 10, as well as a region of high particle concentration along the sides of the particle-filled region. For the cases with adhesion, the particles have formed small ball-like aggregates throughout the flow field. These aggregates are substantially larger near the nodal point at $x = 5$ and within the high-concentration region along the sides of the particle-filled region. Also, the aggregate size is considerably larger for the $\phi = 100$ case than for the $\phi = 10$ case. For instance, in figure 20(a) we plot the time variation of the average number of particles per aggregate for the cases with $\phi = 10$, 40 and 100. The number of particles per aggregate fluctuates with the contractions of the channel walls but in the mean

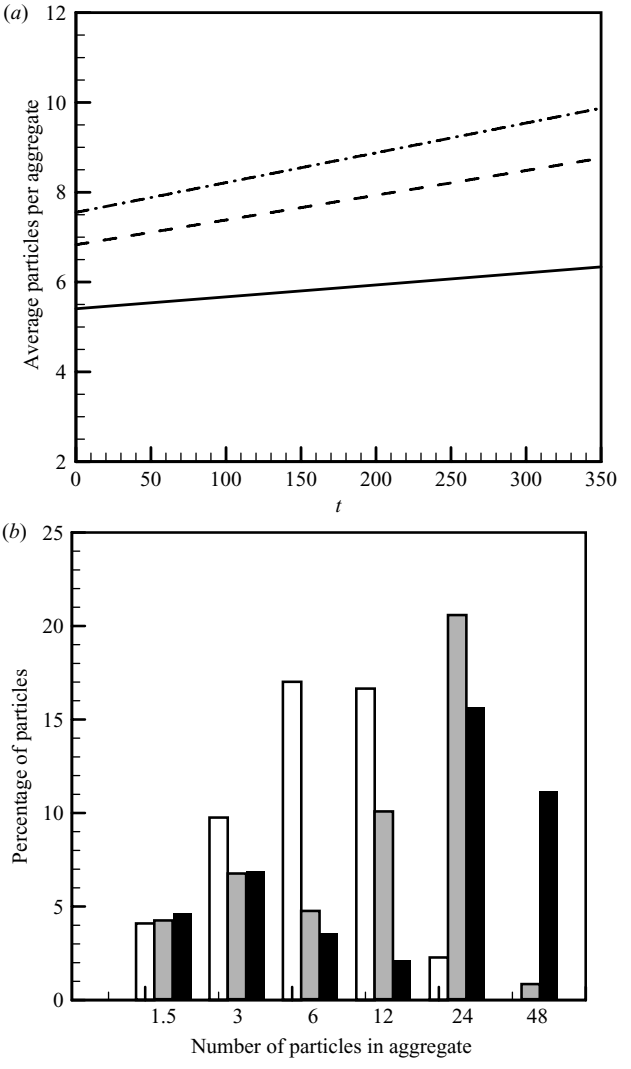

FIGURE 20. Plots for peristaltic waves, showing (*a*) linear fit to average number of particles per aggregate as a function of time for $\phi = 10$ (solid line), 40 (dashed line) and 100 (dashed–dotted line) and (*b*) average distribution of aggregate sizes for $t > 100$ for $\phi = 10$ (white bars), 40 (grey bars) and 100 (black bars).

follows a nearly linear increase with time over the computational period. We have therefore approximated the time variation in both cases with a 'best fit' line.

The distribution of aggregate size, averaged over time for $t > 100$, is illustrated in figure 20(*b*) by plotting the percentage of the total particles contained in aggregates composed of n particles, including particles that are not in an aggregate. The aggregate size is sorted into a series of bins, where the bin width increases logarithmically, and the number written under each bin is the mean of the maximum and minimum values of n for that bin. The limits of each bin are given in table 3, where the largest size aggregate has $n < 64$. The case with $\phi = 10$ exhibits a nearly bell-shaped distribution, with the maximum close to six particles per aggregate. For $\phi = 40$, the number of

Bin number	Range of n
1	$n = 2$
2	$2 < n \leqslant 4$
3	$4 < n \leqslant 8$
4	$8 < n \leqslant 16$
5	$16 < n \leqslant 32$
6	$32 < n \leqslant 64$

TABLE 3. Bins used to show distribution of number of particles per aggregate.

aggregates with 3–16 particles decreases, but there is a substantial increase in the number of aggregates with 16–32 particles per aggregate. The case with $\phi = 100$ has a large number of particles contained in aggregates in the two largest bins, containing 16–64 particles, and a substantial number of particles in aggregates with 2–4 particles but a lower number of particles with aggregates with sizes in between these extremes. The larger bin sizes would seem to correspond to aggregates located along the outside of the channels and near the nodal point at $x = 5$, whereas the smaller bin sizes would appear to correspond to aggregates in the remainder of the flow.

7. Conclusions

We have demonstrated both theoretically and through numerical computations using a DEM that particles suspended in a fluid subjected to oscillating straining cluster around the nodal points of the straining field. While this clustering occurs at all values of the Stokes number, the rate of cluster formation increases with increase in Stokes number. The DEM computations indicate that inclusion of a concentration-dependent friction factor in the particle drag expression causes this clustering to be observed even for certain cases exceeding the stability limit of the associated Matheiu equation. For particles contained in an oscillating box, the inward particle drift due to the oscillating straining flow is ultimately limited by particle contact, leading to formation of a diamond-shaped particle cluster. Computations with particles of different sizes show that the drift rate of the larger particles is faster than that of the smaller particles, such that a separation of particles by size results in which the centre of the resulting cluster is formed of the larger particles, and the sides are coated with the smaller particles. Oscillatory clustering can suspend particles in the presence of a downward gravitational force, where the final state for isolated particles is a limit-cycle oscillation about some mean position which is displaced downward from the straining center. Theoretical predictions for the centroid and oscillation amplitude of this limit cycle are found to be in reasonable agreement with values obtained from DEM simulations for particles in an oscillating box, with differences attributed primarily to the effect of particle crowding on the drag force in the DEM simulations. Computations are performed using DEM for particle transport in a channel with standing wave contractions of the channel walls. The fluid flow is determined using lubrication theory, so the flow Reynolds number is restricted to be relatively small. It is observed that particles within the channel drift towards the nodal points of the straining flow both in the lateral direction and in the direction along the length of the channel.

The cases with an oscillating box and peristaltic standing waves are also examined in the presence of adhesive forces between the particles. For the oscillating box, it is

observed that oscillation of the straining rate causes aggregates to form along the edge of the box, which then propagate inward as dendritic structures, eventually forming a mesh of aggregates that break and reform periodically at certain points in phase with the box oscillations. The particles are observed to initially drift inward somewhat more rapidly in the presence of adhesive forces, but the limiting particle structure is more porous than for the case with no adhesion due to contact and adhesion between the particle aggregates. For the peristaltic oscillations of a channel, particle adhesion is also observed to increase the inward drift of the particles and lead to aggregate formation both within the high-concentration region near the channel walls and in the region near the nodal points of the straining flow.

There are a number of limitations to our numerical method which suggest the need to examine these problems experimentally or with more detailed computational methods in future work. In particular, the flow Reynolds number restriction for the peristaltic wave solution limits the particle Stokes number to fairly small values, for which the particle drift rate is small. Secondly, the fluid flow was assumed to be independent of the particles, which would break down in highly concentrated flows.

Despite these limitations, we can draw some tentative conclusions from our results regarding the importance of the oscillatory clustering phenomenon for several practical problems. For instance, for transport of chyme in the human colon, the contraction frequency is about $\omega \cong 0.05\,\mathrm{s}^{-1}$; the flow Reynolds number is about $Re_F = 10$; and the amplitude ratio is about $\eta = 0.5$ (Gramiak *et al.*, 1971; Brown *et al.*, 1995). The particle Stokes number is related to the dimensionless diameter by $St = \varepsilon^2 Re_F/18\chi$. For very small particles in the colon, with diameter about $d = 0.1$ mm, the dimensionless particle diameter for a section of the colon with $L = 2$ cm radius is $\varepsilon = 0.005$ and the resulting Stokes number is $St = O(10^{-5})$. For particles of this size, the straining parameter is so small that the particle drift due to wall contractions is negligible. The primary effect of the colonic contractions for particles of this size is to increase the collision rate with other small particles, thereby increasing the aggregation rate. On the other hand, for a particle or an aggregate in the colon with diameter of 2 mm, the Stokes number is about 0.005. This Stokes number is about half the value used for the computations in figure 14, which exhibit significant clustering of particles at the nodal points after about 60 wall oscillations. Using the estimate that the drift rate varies approximately with S^2, as indicated by result (2.8), suggests that similar amount of clustering would occur for 2 mm diameter particles in the colon within about 240 oscillations, which using a contraction period of 30 seconds (as is typical of the colon) indicates a time requirement of about 2 hours to produce clustering of 2 mm particles at the nodal points. The drift rate induced by oscillatory clustering therefore acts to transport larger neutrally buoyant particles and aggregates, with diameters of order the of 2 mm or larger, away from the colon walls towards the nodal points of the straining flow within the tube centre, thus aiding in clearing these larger particles and aggregates away from the region in which water is withdrawn through the colon walls.

In engineering systems, we can manipulate the oscillation frequency to increase the Stokes number, thereby increasing the particle drift rate. For instance, for a 1 mm diameter aggregate of algae cells immersed in water, the Stokes number is about 0.1 when the oscillation frequency is only $\omega = 3.6\,s^{-1}$, corresponding to an oscillation period of about 2 seconds. The corresponding value of the straining parameter at the nodal point is $S = 3\eta\, St \cong 0.1$ with an amplitude ratio of about $\eta \cong 0.3$, for which case our computations indicate that an algae solution would quickly form clusters at the straining nodal points of the flow.

One of the interesting aspects of the oscillatory clustering phenomenon is that for aqueous solutions it is most effective for particles in the range of 1 mm diameter, yielding particle Stokes numbers in the range of 0.1–0.5. The reason for the dominance of this range of Stokes number is that the clustering phenomenon is an artefact of the particle inertial overshoot, so it is most effective for cases with significant particle inertia. The acoustic radiation force resulting from ultrasound waves, on the other hand, has been widely used for biological cells and for particles in micro-channels, with particle diameters of the order of 10 μm. Particles this small have very small Stokes numbers, so the oscillatory clustering phenomenon is not generally as effective. These two approaches are therefore complementary to each other and might be used either singly or in unison to induce clustering and aggregation for a wide range of particle sizes.

The author thanks H. S. Udaykumar, K. Schulze-Delrieu and S. Krishnan for many enjoyable conversations at the University of Iowa on intestinal fluid flows and particle transport, which motivated this investigation. Funding was provided by the US Department of Transportation via grant number DTOS59–06-G-00048 and by Vermont EPSCoR via grant number EPS 0701410.

REFERENCES

Bagi, K. & Kuhn, M. R. 2004 A definition of particle rolling in a granular assembly in terms of particle translations and rotations. *J. Appl. Mech.* **71**, 493–501.

Bar-Cohen, Y. & Chang, Z. 2000 Piezoelectrically actuated miniature peristaltic pump. In *Proc. SPIE Conf. on Smart Structures and Materials*, Newport Beach, California.

Brasseur, J. G., Corrsin, S. & Lu, N. Q. 1987 The influence of a peripheral layer of different viscosity on peristaltic pumping with Newtonian fluid. *J. Fluid Mech.* **174**, 495–519.

Brown, B. P., Schrier, J. E., Berbaum, K. S., Shirazi, S. S. & Shulze-Delrieu, K. 1995 Haustral septations increase axial and radial distribution of luminal contents in glass models of the colon. *Am. J. Physiol.* **269**, G706–G709.

Chokshi, A., Tielens, A. G. G. M. & Hollenbach, D. 1993 Dust coagulation. *Astrophys. J.* **407**, 806–819.

Cleary, P. W., Metcalfe, G. & Liffman, K. 1998 How well do discrete element granular flow models capture the essentials of mixing processes? *Appl. Math. Mod.* **22**, 995–1008.

Di Felice, R. 1994 The voidage function for fluid–particle interaction systems. *Intl J. Multiphase Flow* **20**, 153–159.

Dominik, C. & Tielens, A. G. G. M. 1995 Resistance to rolling in the adhesive contact of two elastic spheres. *Philos. Mag.* A **92** (3), 783–803.

Dominik, C. & Tielens, A. G. G. M. 1997 The physics of dust coagulation and the structure of dust aggregates in space. *Astrophys. J.* **480**, 647–673.

Fauci, L. J. 1992 Peristaltic pumping of solid particles. *Comp. Fluids* **21** (4), 583–598.

Ferry, J., Rani, S. L. & Balachandar, S. 2003 A locally implicit improvement of the equilibrium Eulerian method. *Intl J. Multiphase Flow* **29**, 869–891.

Gallego-Juárez, J. A., de Sarabia, E. R. F., Rodrígues-Corral, G., Hoffman, T., Gálvez-Moraleda, J. C., Rodrígues-Maroto, J. J., Gómez-Moreno, F. J., Bahillo-Ruiz, A., Martin-Espigares, M. & Acha, M. 1999 Application of acoustic agglomeration to reduce fine particle emissions from coal combustion plants. *Environ. Sci. Technol.* **33**, 3943–3849.

Gramiak, R., Ross, P. & Olmstead, W. W. 1971 Normal motor activity of the human colon: combined radiotelemetric manometry and slow-frame cineroentgenography. *Am. J. Roentgenol. Radium Ther. Nucl. Med.* **113** (2), 301–309.

Gunderson, H., Rigas, H. & van Vleck, F. S. 1974 A technique for determining stability regions for the damped Mathieu equation. *SIAM J. Appl. Math.* **26** (2), 345–349.

Hartley, F. T. 2000 Miniature peristaltic pump technology and applications. *J. Advanced Mater.* **32** (3), 16–22.

Hertz, H. 1882 Über die Berührung fester elastische Körper. *J. Reine Angew. Math.* **92**, 156–171.

Hung, T. K. & Brown, T. D. 1976 Solid-particle motion in two-dimensional peristaltic flows. *J. Fluid Mech.* **73**, 77–96.

Jaffrin, M. Y. 1973 Inertia and streamline curvature effects on peristaltic pumping. *Intl J. Engng Sci.* **11** (6), 681–699.

Jaffrin, M. Y. & Shapiro, A. H. 1971 Peristaltic pumping. *Annu. Rev.Fluid Mech.* **3**, 13–36.

Johnson, K. L., Kendall, K. & Roberts, A. D. 1971 Surface energy and the contact of elastic solids. *Proc. R. Soc. London* A **324**, 301–313.

Joseph, G. G., Zenit, R. Hunt, M. L. & Rosenwinkel, A. M. 2001 Particle–wall collisions in a viscous fluid. *J. Fluid Mech.* **433**, 329–346.

Jouet, P., Coffin, B., Lémann, M., Gorbatchef, C., Franchisseur, C., Jian, R. Rambaud, J.-C. & Flourié, B. 1998 Tonic and phasic motor activity in the proximal and distal colon of healthy humans. *Am. J. Physiol. Gastrointest. Liver Physiol.* **274**, 459–464.

Kapishnikov, S., Kantsler, V. & Steinberg, V. 2006 Continuous particle size separation and size sorting using ultrasound in a microchannel. *J. Stat. Mech.*, P01012.

King, L. V. 1934 On the acoustic radiation pressure on spheres. *Proc. Royal Soc. London* A **147**, 212–240.

Kuznetsova, L. A., Bazou, D. & Coakley, W. T. 2007 Stability of 2-D colloidal particle aggregates held against flow stress in an ultrasound trap. *Langmuir* **23**, 3009–3016.

Lew, H. S., Fung, Y. C. & Lowenstein, C. B. 1971 Peristaltic carrying and mixing of chyme in the small intestine (an analysis of a mathematical model of peristalsis of the small intestine). *J. Biomech.* **4**, 297–315.

Li, M. & Brasseur, J. G. 1993 Nonsteady peristaltic transport in finite-length tubes. *J. Fluid Mech.* **248**, 129–152.

Li, S. Q. & Marshall, J. S. 2007 Discrete-element simulation of micro-particle deposition on a cylindrical fiber in an array. *J. Aerosol Sci.* **38**, 1031–1046.

Marshall, J. S. 2006 Effect of shear-induced migration on the expulsion of heavy particles from a vortex core. *Phys. Fluids* **18** (11), 113301-1–113301-12.

Marshall, J. S. 2007 Particle aggregation and capture by walls in a particulate aerosol channel flow. *J. Aerosol Sci.* **38**, 333–351.

Maxey, M. R. & Riley, J. J. 1983 Equation of motion for a small rigid sphere in a non-uniform flow. *Phys. Fluids* **24**, 883–889.

McLachlan, N. W. 1951 *Theory and Application of Mathieu Functions.* Oxford University Press.

Mindlin, R. D. 1949 Compliance of elastic bodies in contact. *J. Applied Mech.* **16**, 259–268.

Mousel, J. 2006 A computational investigation of particle aggregate growth in micro-nozzles using discrete-element modeling. MS thesis, University of Iowa.

Natarajan, S. & Mokhtarzadeh-Dehghan 2000 Numerical prediction of flow in a model of a (potential) soft acting peristaltic blood pump. *Intl J. Numer. Methods Fluids* **32** (6), 711–724.

Nguyen, N. T., Huang, X. & Chuan, T. K. 2002 MEMS-micropumps: a review. *J. Fluids Enging* **124**, 384–392.

Pal, A. & Brasseur, J. G. 2000 There is more to longitudinal shortening than physiology. *Gastroenterology* **118** (4), A385–A385.

Pal, A. & Brasseur, J. G. 2002 The mechanical advantage of local longitudinal shortening on peristaltic transport. *J. Biomech. Engng* **124** (1), 94–100.

Pritchard, A. J. 1969 Stability of the damped Mathieu equation. *Elec. Lett.* **5** (26), 700–701.

Pozrikidis, C. 1987 A study of peristaltic flow. *J. Fluid Mech.* **180**, 515–527.

Putz, R. & Pabst, R. 2000 *Sobotta Atlas of Human Anatomy*, vol. 2, 13th ed. Lippincott, Williams and Wilkins.

Ramachandra Rao, A. & Usha, S. 1995 Peristaltic transport of two immiscible viscous fluids in a circular tube. *J. Fluid Mech.* **298**, 271–285.

Rathish Kumar, B. V. & Naidu, K.B. 1995 A numerical study of peristaltic flows. *Comput. Fluids* **24** (2), 161–176.

Robe, T. R. & Jones, S. E. 1975 A numerical method for establishing Liapunov stability of linear second order non-autonomous dynamical systems. *J. Inst. Math. Appl.* **16**, 109–120.

Savkoor, A. R. & Briggs, G. A. D. 1977 The effect of tangential force on the contact of elastic solids in adhesion. *Proc. R. Soc. London* A **356**, 103–114.

Schulze-Delrieu, K., Brown, B. P., Lange, W., Custer-Hagan, T., Lu, C., Shirazi, S. & Lepsien, G. 1996 Volume shifts, unfolding and rolling of haustra in the isolated guinea pig caecum. *Neurogstroenterol. Mot*. **8**, 217–225.

Serayssol, J.-M. & Davis, R. H. The influence of surface interactions on the elastohydrodynamic collision of two spheres. *J. Colloid Interface Sci.* **114** (1), 54–66.

Shapiro, A. H., Jaffrin, M. Y. & Weinberg, S. L. 1969 Perisaltic pumping with long wavelengths at low Reynolds numbers. *J. Fluid Mech.* **37**, 799–825.

Shukla, J. B., Parihar, R. S., Rao, B. R. P. & Gupta, S. P. 1980 Effects of peripheral-layer viscosity on peristaltic transport of a bio-fluid. *J. Fluid Mech.* **97**, 225–237.

Spengler, J. F., Jekel, M., Christensen, K. T., Adrian, R. J., Hawkes, J. J. & Coakley, W. T. 2001 Observation of yeast cell movement and aggregation in a small-scale MHz-ultrasonic standing wave field. *Bioseparation* **9**, 329–341.

Srivastava, L. M. & Srivastava, V. P. 1989 Peristaltic transport of a particle-fluid suspension. *J. Biomech. Engng* **111** (2), 157–165.

Srivastava, V. P. & Srivastava, L. M. 1997 Influence of wall elasticity and Poiseuille flow on peristaltic induced flow of a particle-fluid mixture. *Intl J. Engng Sci.* **35** (15), 1359–1386.

Takabatake, S. & Ayukawa, K. 1982 Numerical study of two-dimensional peristaltic flows. *J. Fluid Mech.* **122**, 439–465.

Taylor, J. H. & Narendra, K. S. 1969 Stability regions for the damped Mathieu equation. *SIAM J. Appl. Math.* **17** (2), 343–352.

Thornton, C. 1991 Interparticle sliding in the presence of adhesion. *J. Phys.*D **24**, 1942–1946.

Tsuji, Y., Tanaka, T. & Ishida, T. 1992 Lagrangian numerical simulation of plug flow of cohesionless particles in a horizontal pipe. *Powder Technol.* **71**, 239–250.

Usha, S. & Ramachandra Rao, A. 1997 Peristaltic transport of two-layered power-law fluids. *J. Biomed. Engng* **119** (4), 483–488.

Usha, S. & Ramachandra Rao, A. 2000 Effects of curvature and inertia on the peristaltic transport in a two-fluid system. *Intl J. Engng Sci.* **38** (12), 1355–1375.

Zhao, Y. & Marshall, J. S. 2008 Spin coating of a colloidal suspension. *Phys. Fluids* **20** (4), 043302-1–043302-15.